REPORT DOCUMENTATION PAGE

Form Approved OMB NO. 0704-0188

1. REPORT DATE (DD-MM-YYYY)	2. REPORT TYPE	3. DATES COVERED (From - To)
30-10-2019	Final Report	1-Jun-2015 - 30-Jun-2019

4. TITLE AND SUBTITLE
Final Report: Photon Statistics and Spectral Selectivity Limits of Thermal Detectors

5a. CONTRACT NUMBER
W911NF-15-1-0243

5b. GRANT NUMBER

5c. PROGRAM ELEMENT NUMBER
611102

6. AUTHORS

5d. PROJECT NUMBER

5e. TASK NUMBER

5f. WORK UNIT NUMBER

7. PERFORMING ORGANIZATION NAMES AND ADDRESSES
University of Minnesota - Minneapolis
450 McNamara Alumni Center
200 Oak Street SE
Minnepolis, MN 55455 -2070

8. PERFORMING ORGANIZATION REPORT NUMBER

9. SPONSORING/MONITORING AGENCY NAME(S) AND ADDRESS (ES)
U.S. Army Research Office
P.O. Box 12211
Research Triangle Park, NC 27709-2211

10. SPONSOR/MONITOR'S ACRONYM(S)
ARO

11. SPONSOR/MONITOR'S REPORT NUMBER(S)
66979-EL.5

12. DISTRIBUTION AVAILIBILITY STATEMENT
Approved for public release; distribution is unlimited.

13. SUPPLEMENTARY NOTES
The views, opinions and/or findings contained in this report are those of the author(s) and should not contrued as an official Department of the Army position, policy or decision, unless so designated by other documentation.

14. ABSTRACT

15. SUBJECT TERMS

16. SECURITY CLASSIFICATION OF:			17. LIMITATION OF ABSTRACT	15. NUMBER OF PAGES	19a. NAME OF RESPONSIBLE PERSON
a. REPORT	b. ABSTRACT	c. THIS PAGE			Joseph Talghader
UU	UU	UU	UU		19b. TELEPHONE NUMBER 612-625-4524

RPPR Final Report
as of 31-Oct-2019

Agency Code:

Proposal Number: 66979EL **Agreement Number: W911NF-15-1-0243**
INVESTIGATOR(S):

Name: Joseph Talghader
Email: joey@umn.edu
Phone Number: 6126254524
Principal: Y

Organization: **University of Minnesota - Minneapolis**
Address: 450 McNamara Alumni Center, Minnepolis, MN 554552070
Country: USA
DUNS Number: 555917996 EIN: 41-6007513

Report Date: 30-Sep-2019 Date Received: 30-Oct-2019
Final Report for Period Beginning 01-Jun-2015 and Ending 30-Jun-2019
Title: Photon Statistics and Spectral Selectivity Limits of Thermal Detectors
Begin Performance Period: 01-Jun-2015 **End Performance Period:** 30-Jun-2019
Report Term: 0-Other

Submitted By: Joseph Talghader Email: joey@umn.edu
Phone: (612) 625-4524

STEM Degrees: 3 **STEM Participants:** 5

Major Goals: The three primary goals of the program have remained largely the same throughout the program, and we need only slightly modify and abridge the original proposal text to write:

1) Model the contribution of Bose-Einstein statistics to the photon noise of radiation-limited thermal detectors, for both single radiation mode and multimode detectors.

2) Theoretically and experimentally quantify the dominant phenomena that cause uncertainty or fluctuations in the rest position of a thermal detector. For devices with high sensitivity and spectral resolution, these will include photon counting noise, and thermomechanical noise.

3) Develop radiation noise theory for extremely narrow spectrum thermal detectors that includes an accounting of the cavity-altered density of states.

Accomplishments: See uploaded document.

RPPR Final Report
as of 31-Oct-2019

Training Opportunities:
Over the course of the program, three primary graduate students have been trained: Kyle Olson, Yu-Jen Lee, and Eric Konitzer. Kyle Olson and Yu-Jen Lee were primarily involved with the theory of photon statistics and radiation noise. Kyle Olson wrote an important paper for Physical Review that generalized previous photon statistics for radiation noise to any spectrally selective detector. Dr. Olson graduated with his PhD from the University of Minnesota in December 2015. Yu-Jen then began exploring techniques for microfabricating microresonators to create high Q optical cavities. As part of this he experimenting with new materials, particularly diamond, that have sufficiently low loss in the LWIR to create cavity quality factors greater than 1000, and order of magnitude better than previously published. Yu-Jen is expected to graduate with his PhD in February 2020. Eric Konitzer graduated with his Masters degree from Minnesota in May 2019. He investigated buckling and thermomechanical noise properties of optomechanical infrared detectors and performed both theoretical and experimental work in this area.

In summer 2018, an undergraduate at the University of Minnesota, Brock Grafstrom, participated in our program as an ARO UROP participant. This went very well as Brock received training in materials, microfabrication, and thermomechanical noise characterization. The work of this program was reported by a student at the First Diamond Photonics Conference in Lausanne. In addition, a Senior Honors, undergraduate student, Marley Stephens, participated in the project, learning both microfabrication and modeling and presenting his work at multiple Senior Honors presentations.

Kyle Olson received his PhD from the University of Minnesota in December 2015 with the thesis, "High Power Continuous Wave Laser Heating and Damage with Contamination, and Non-Uniform Spectrally Dependent Thermal Photon Statistics."

Eric Konitzer graduated with his Master's degree from the University of Minnesota in May 2018. He now works on directed energy and other DoD related topics at the Applied Physics Laboratory in Maryland.

RPPR Final Report
as of 31-Oct-2019

Results Dissemination:
The following journal papers have been published:

K. Olson, and J. Talghader “Spectrally dependent fluctuations of thermal photon sources, Physical Review A, vol. 94, 013822, 5 pages, 2016.

Y. J. Lee and J. J. Talghader, “Observational limitations of Bose-Einstein photon statistics and radiation noise in thermal emission,” Physical Review A, vol. 97, 013844 (11 pages), 26 January 2018. DOI: 10.1103/PhysRevA. 97.013844

Based on the experimental work of the last year of the program, we achieved further significant results and currently have a publication going through the journal review cycle plus one other in preparation.

We also have the following conference publication based on our
earliest LWIR microresonators results:

Y.-J. Lee, A. Das, and J. J. Talghader, "Long-Wave Infrared Diamond Microdisk High-Q Resonator," Symposium Latsis 2019 on Diamond Photonics, Lausanne, May 19-22, 2019, pp. 21-22.

In addition, Professor Talghader has given several invited talks at academic conferences, DoD forums, universities, and industry including (but not only)

J. J. Talghader, "Future Directions for Microbolometers and Thermopile Infrared Detectors," Image Sensing Technologies: Materials, Devices, Systems, and Applications V in SPIE Defense and Commercial Sensing, Orlando, FL, April 2018.

J. J. Talghader, "Future Directions for Uncooled Infrared Detectors," DoD Basic Research Forum, Arlington, VA, October 19, 2017.

J. J. Talghader, "Revisiting Planck’s Law: Thermal Emission and Radiation Noise in Subwavelength Infrared Cavities," Conference on Lasers and Electrooptics Pacific Rim, Oral 3-2F-1, Singapore, August 3, 2017.

J. J. Talghader, “Microsensors and Particles: Infrared detectors, solar driven devices, and sensing inside explosions,” Stanford Photonics Research Conference, Stanford, CA, September 19-20, 2016.

J. J. Talghader, “Physical Limits of Thermal Infrared Detection”, IEEE Sensors Conference, Busan, South Korea, November 1-4, 2015.

Other related talks were given at the University of Texas, Penn State University, Rice University, the University of Southern California, and Halliburton

During the program, Professor Talghader has interacted with Raytheon on technology and proposal submission. In addition, Prof. Talghader also gave a presentation for the Raytheon uncooled detector group. J. Talghader, "Future Directions for Uncooled Infrared Detectors," Raytheon Vision Systems, Goleta, CA, November 9, 2018.

Honors and Awards: Kyle Olson was awarded a PhD from the University of Minnesota in December 2015 with the thesis, "High Power Continuous Wave Laser Heating and Damage with Contamination, and Non-Uniform Spectrally Dependent Thermal Photon Statistics."

Eric Konitzer was awarded a Master's degree from the University of Minnesota in May 2019.

Protocol Activity Status:

RPPR Final Report
as of 31-Oct-2019

Technology Transfer:
During the program, Professor Talghader has interacted with Raytheon on technology and proposal submission (new materials that can reduce 1/f noise and overcome thermal/electrical conductivity limitations given by the Wiedemann-Franz Law for common metals). In addition, Prof. Talghader also gave a presentation for the Raytheon uncooled detector group. J. Talghader, "Future Directions for Uncooled Infrared Detectors," Raytheon Vision Systems, Goleta, CA, November 9, 2018.

PARTICIPANTS:

Participant Type: PD/PI
Participant: Joseph John Talghader
Person Months Worked: 4.00 **Funding Support:**
Project Contribution:
International Collaboration:
International Travel:
National Academy Member: N
Other Collaborators:

Participant Type: Graduate Student (research assistant)
Participant: Kyle Olson
Person Months Worked: 6.00 **Funding Support:**
Project Contribution:
International Collaboration:
International Travel:
National Academy Member: N
Other Collaborators:

Participant Type: Graduate Student (research assistant)
Participant: Yu-Jen Lee
Person Months Worked: 15.00 **Funding Support:**
Project Contribution:
International Collaboration:
International Travel:
National Academy Member: N
Other Collaborators:

Participant Type: Graduate Student (research assistant)
Participant: Eric Konitzer
Person Months Worked: 9.00 **Funding Support:**
Project Contribution:
International Collaboration:
International Travel:
National Academy Member: N
Other Collaborators:

Participant Type: Undergraduate Student
Participant: Brock Grafstrom
Person Months Worked: 3.00 **Funding Support:**
Project Contribution:
International Collaboration:
International Travel:
National Academy Member: N
Other Collaborators:

RPPR Final Report
as of 31-Oct-2019

Participant Type: Undergraduate Student
Participant: Marley Stephens
Person Months Worked: 7.00 **Funding Support:**
Project Contribution:
International Collaboration:
International Travel:
National Academy Member: N
Other Collaborators:

CONFERENCE PAPERS:

Publication Type: Conference Paper or Presentation **Publication Status:** 1-Published
Conference Name: Symposium Latsis 2019 on Diamond Photonics
Date Received: 02-Sep-2019 Conference Date: 19-May-2019 Date Published: 19-May-2019
Conference Location: Lausanne, Switzerland
Paper Title: Long-Wave Infrared Diamond Microdisk High-Q Resonator
Authors: Y.-J. Lee, A. Das, and J. J. Talghader
Acknowledged Federal Support: **Y**

DISSERTATIONS:

Publication Type: Thesis or Dissertation
Institution: University of Minnesota
Date Received: 27-Aug-2016 Completion Date: 1/1/16 9:43AM
Title: High Power Continuous Wave Laser Heating and Damage with Contamination, and Non-Uniform Spectrally Dependent Thermal Photon Statistics
Authors: Kyle Olson
Acknowledged Federal Support: **Y**

Contract Number: W911NF-15-1-0243

Title: Photon Statistics and Spectral Selectivity Limits of Thermal Detectors

Summary of Primary Findings

To frame the discussion, we will repeat the primary goals of the program as derived from the original program proposal:

1) Model and measure the contribution of Bose-Einstein statistics to the photon noise of radiation-limited thermal detectors, for both single radiation mode and multi-mode detectors.
2) Theoretically and experimentally quantify the dominant phenomena that cause uncertainty or fluctuations in the rest position of a thermal detector. For devices with high sensitivity and spectral resolution, these will, at a minimum, include photon counting noise, and thermomechanical noise.
3) Develop radiation noise theory for extremely narrow spectrum thermal detectors that includes an accounting of the cavity-altered density of states. Experimentally, this provides an intriguing opportunity to study how modes internal to the detector couple to free space modes.

Table of Contents (Total 53 pages)

PART I: Photon Statistics of a Thermal Detector with an Arbitrary Distribution of Modes

This section primarily discusses goals 1 and 2, although the recently published solution for goal 1 [1,2] also overlaps goal 3. **The reason that goal 1 is important is that the ultimate performance of infrared devices, given by the radiation background limit, depends directly on the photon fluctuations in a device. The background limit is different for a device interacting with many modes and a device interacting with only one mode. While these two extremes were known, there was no general expression for photon fluctuations for few modes or modes of variable coupling to free space. Now that problem has been solved and in the next year we will be developing the new radiation background noise theory as a performance limit for micro- and nano-cavity devices.**

60 year old problem in physics is solved, revealing the noise signature of confined light [1].

The noise signature in thermal light sources, such as microcavity devices or stars, obey an equation developed in the 60's whose general solution has eluded scientists, until now. All objects heated above absolute zero emit an enormous spectrum of light into an equally large amount of allowed spatial patterns called "modes". At short wavelengths, in the visible and ultraviolet, most modes are devoid of photons, but deep in the infrared there are many photons per mode. In traditional optical devices, this difference between short and long wavelength has little impact on device performance because all of the modes average together.

However, if the volume of space around the heated object, such as an infrared detector, is very small, the number of modes becomes small, and the number of long-wavelength photons in each mode fluctuates in a way given by Bose-Einstein quantum statistics instead of the more typical Poisson. This means that the device noise and performance fundamentally changes for optical devices that interact with a small number of modes at long wavelengths. Olson and Talghader describe an analytical solution for the general case, matching precisely with intensive numerical calculations. The method used in finding the elusive solution could be used to solve further unresolved questions in detector physics, mathematics, and other STEM fields.

Detailed Description

The development of microcavities of dimensions comparable to wavelength [3–7], such as in coherent thermal emission [5,7–12], narrowband thermal detection [3,6,13], and cavity quantum electrodynamics [14–20] has opened an entire class of devices whose thermal statistics cannot be addressed by existing theory. Thermal light emitted into free space generally interacts with an enormous spectral density of modes. The photon number fluctuations of thermal emission into each mode have Poisson and Bose-Einstein contributions, but the latter average out when integrated over many modes, leaving only standard Poisson statistics. Historically, since almost all thermal emission occurred in systems with large numbers of modes, it has not been important to have a quantitative model of photon statistics for a small number; however, the aforementioned experimental and theoretical work in cavity micro- and nano-optics has changed this situation dramatically.

A microcavity can define an enormous variety of mode distributions, and the strength of coupling between these modes and free space can vary from mode to mode. An analytical derivation of the thermal photon noise for the general case of an arbitrary number of modes with an arbitrary spectral distribution (determined by both the Planck distribution and the mode coupling) has eluded scientists since the late 1950's due to the complicated mathematics at hand [21–25]. We propose and demonstrate using an expansion of the probability density function to analytically find an exact general result for thermal photon population fluctuations for any average number of photons in any number of modes with any spectral dependence. This method sidesteps many of the mathematical complexities of previous treatments and produces a closed-form result.

Thermal photons will have number fluctuations given by the sum of Poisson and Bose-Einstein (B-E) terms in single mode systems. The B-E contribution will be reduced to zero when integrated over many modes resulting in only Poisson statistics for most thermal light. If there are multiple modes but the spectrum is completely uniform, then the variance in the number fluctuations can be given by the following equation [21,26].

$$\langle (\Delta n)^2 \rangle = \langle n \rangle + \frac{\langle n \rangle^2}{M} \quad (1)$$

In Eq. (1) n is the number of photons, $\langle n \rangle$ is the expected number of photons, M is the

number of modes, and $\langle(\Delta n)^2\rangle$ is the variance.

Following an algorithm developed previously [27], the general probability density for thermal photons is given by the following equation.

$$P(n)=\sum_{d=1}^{D}\prod_{m=1}^{M}\frac{1}{\left(1+\langle n_m\rangle\right)\left(1+\langle n_m\rangle^{-1}\right)^{n_{m,d}}} \quad (2)$$

In Eq. (2) and the rest of the manuscript the following variables are defined as the following: n is the number of photons; m indicates the mode index; $\langle n_{\mathrm{m}}\rangle$ is the average number of photons in mode m; d indicates the distribution index; $P(n)$ denotes the probability of having n photons given $\langle n_{\mathrm{m}}\rangle$; M is the total number of modes; D is the total number of ways to distribute n photons in M modes; $n_{m,d}$ denotes the number of photons in mode m and distribution d; $\langle n\rangle$ is the average total number of photons; $\langle(\Delta n)^2\rangle$ is the variance in the total number of photons.

Note that n is the discrete random variable, in other words, for $n = 0$, Eq. (2) computes the probability of having 0 photons given the distribution $\langle n_{\mathrm{m}}\rangle$. The number of possible photon distributions, D, is given by,

$$D=\frac{(n+M-1)!}{n!(M-1)!} \quad (3)$$

GENERAL SPECTRALLY DEPENDENT MODE DISTRIBUTIONS

To find the variance of general spectrally dependent thermal photon statistics, we first need to find an expression for the mode distribution scaled to the total average photon number. The scaled mode distribution in the general case can be visualized in Fig. 1. Naturally, the sum of the average photon number in each mode equals the total average photon number, but it is convenient to normalize a scaled distribution to the total average photon number such that the distribution is a function of the total average photon number.

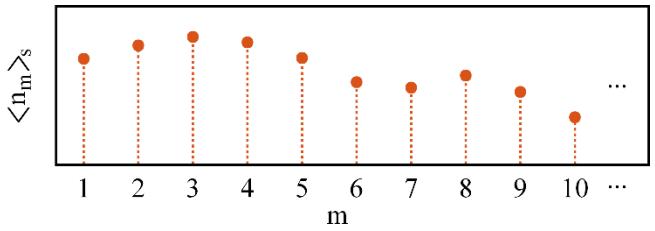

FIG. 1. General spectrally dependent mode distributions; the subscript "s" signifies that this distribution is scaled, and that the sum does not equal the total average photon number.

The sum of the average photon number in the modal distribution, $\langle n_{\mathrm{m}} \rangle$, is equal to the expected number of photons, $\langle n \rangle$, as in the following equations,

$$\langle n \rangle = \sum_{m=1}^{M} \langle n_m \rangle = \sum_{m=1}^{M} A \langle n_m \rangle_s \quad (4)$$

$$A = \frac{\langle n \rangle}{\sum_{m=1}^{M} \langle n_m \rangle_s} \quad (5)$$

$$\langle n_m \rangle = \frac{\langle n \rangle \langle n_m \rangle_s}{\sum_{m=1}^{M} \langle n_m \rangle_s} \quad (6)$$

The scaling factor A in Eq. (4) scales the modal distribution to a normalized value as in Eq. (6). Now that there is an expression for the general mode distribution we can plug this into Eq. (2) and solve for the probability of having 0 or 1 photon in the system.

$$P(0) = \prod_{m=1}^{M} \frac{1}{\left(1 + \frac{\langle n \rangle \langle n_m \rangle_s}{\sum_{m=1}^{M} \langle n_m \rangle_s}\right)} \quad (7)$$

$$P(1) = \sum_{d=1}^{M} \prod_{m=1}^{M} \frac{1}{\left(1 + \frac{\langle n \rangle \langle n_m \rangle_s}{\sum_{m=1}^{M} \langle n_m \rangle_s}\right)\left(1 + \frac{\sum_{m=1}^{M} \langle n_m \rangle_s}{\langle n \rangle \langle n_m \rangle_s}\right)^{\delta_{m,d}}} \quad (8)$$

$$P(2) \cong 1 - P(1) - P(0) \quad (9)$$

$$P(n > 2) \cong 0 \quad (10)$$

These probabilities are accurate for average photon numbers much less than one. However, notice that it is the scaling factor that has forced the photon number to this low value. We

will later consider the limit as the average photon number approaches zero to recover the analytical result, and then adjust the scaling factor to show that it applies to all photon numbers, low and high.

With the above probabilities, the variance in the signal can be found for small expected photon numbers. Using standard statistical techniques the variance is defined by the following equation.

$$\langle (\Delta n)^2 \rangle = \sum_{n=0}^{2} \left(n - \langle n \rangle \right)^2 P(n) \quad (11)$$

From Eq. (1) it is reasoned that the variance must have a lower limit defined by Poissonian statistics in the case of infinite modes, and an upper limit defined by the sum of both Poissonian and B-E terms in the case of a single mode. It follows then that the variance can be scaled and normalized by the following equation to force the variance between the limits of zero and one.

$$\overline{\langle (\Delta n)^2 \rangle} = \frac{\langle (\Delta n)^2 \rangle - \langle n \rangle}{\langle n \rangle^2} \quad (12)$$

From the normalized and scaled variance, finding the limit as the average photon number goes to zero can now be attempted. Solving the equation would be quite difficult, instead a limit-based approach is presented whereby the solution is found.

The first thing to notice is that in most cases where spectrally dependent thermal photon noise will be critical, the number of modes will be small. This is because in systems with large number of modes the statistics will approach Poissonian statistics, and the spectral dependence will become negligible. Therefore, the number of modes, *M*, will be set to one and the limit will be found. The number of modes will then be increased and a new limit will be found. This will continue until a fit is found for the limit as a function of the number of modes. The limit of the normalized and scaled variance as the average photon number goes to zero is found to be given by the following equation.

$$\lim_{\langle n \rangle \to 0} \left(\overline{\langle (\Delta n)^2 \rangle} \right) = \frac{\sum_{m=1}^{M} \langle n_m \rangle_s^{\,2}}{\left(\sum_{m=1}^{M} \langle n_m \rangle_s \right)^2} \quad (13)$$

Equation (13) was verified and confirmed to be exactly correct for $1 \leq M \leq 36$ modes with *Mathematica* for any photon distribution $\langle n_m \rangle_s$ with any photon occupancy greater than 0. Systems with greater than 36 modes could not be solved exactly, but it is strongly implied that Eq. (13) is exactly correct for any arbitrarily large number of modes. To verify this assumption further the limit can be solved numerically with some certain defined spectrums with more than 36 modes, and no spectrums were found to not obey Eq. (13). More importantly Eq. (13) is exactly correct for any photon occupancy, even when the B-E term dominates with an average photon occupancy greater than 1.

De-normalizing the result in Eq. (13) can be completed by substituting the result into Eq. (12) and solving for the variance. Doing so results in the following general theory of thermal photon statistics.

$$\langle (\Delta n)^2 \rangle = \langle n \rangle + \langle n \rangle^2 \frac{\sum_{m=1}^{M} \langle n_m \rangle_s^{\,2}}{\left(\sum_{m=1}^{M} \langle n_m \rangle_s \right)^2} \quad (14)$$

It can be shown that Eq. (14) reduces to the standard estimation given in Eq. (1) for a uniform spectrum.

DISCUSSION

Equation (14) can be simplified further by noticing that a physical mode distribution is actually just the scaled mode distribution with a scaling factor equal to one. In this case we can simplify the general theory of thermal photon statistics as in the following equations.

$$\langle (\Delta n)^2 \rangle = \langle n \rangle + \langle n \rangle^2 \frac{\sum_{m=1}^{M} \langle n_m \rangle^2}{\left(\sum_{m=1}^{M} \langle n_m \rangle \right)^2} \quad (15)$$

By substituting Eq. (4) into (15) the following simplifications can be made.

$$\begin{aligned}\langle(\Delta n)^2\rangle &= \sum_{m=1}^{M}\langle n_m\rangle \\ &\quad + \left(\sum_{m=1}^{M}\langle n_m\rangle\right)^2 \frac{\sum_{m=1}^{M}\langle n_m\rangle^2}{\left(\sum_{m=1}^{M}\langle n_m\rangle\right)^2} \qquad (16)\\ &= \sum_{m=1}^{M}\langle n_m\rangle + \sum_{m=1}^{M}\langle n_m\rangle^2 \\ &= \sum_{m=1}^{M}\langle n_m\rangle + \langle n_m\rangle^2\end{aligned}$$

What is proved by Eq. (16) is that spectrally dependent thermal photon statistics are very simple to compute with a general closed-form expression. The variance in photon number for a thermal source is given by the sum of the variances of each individual mode. This also means the covariance between any two modes is zero for thermal photons.

As an example of how important this result can be, we calculate the thermal noise in the emission spectrum of an absorbing Fabry-Pérot cavity, as plotted in Fig. 2. When the cavity with this mode distribution is heated, it will emit thermal radiation defined by the spectral emissivity of the cavity multiplied by Planck's law of thermal radiation. The peaks generated by the cavity can be thought of as different thermal emission modes. Integrating over each peak will produce the photon mode distribution to be modeled.

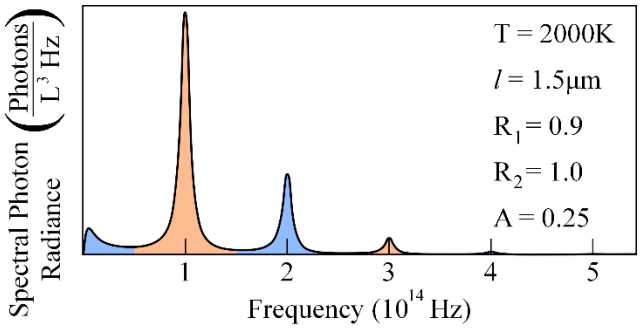

FIG. 2. Spectral Photon Radiance of a thermal source at 2000K in a microcavity, calculated for normal incident light. R_1 and R_2 are the reflectivities of the top and bottom cavity mirrors respectively, A is the single pass absorption of the cavity, and l is the thickness of the cavity. The discrete modal spectral distribution can be calculated by integrating over each peak as highlighted, and is decidedly non-uniform.

The number of modes can be estimated by the following equation [22].

$$M \approx \frac{8\pi\nu^2\mu^3 V}{c^3} d\nu \quad (17)$$

In Eq. (17), μ is the index of refraction in the middle of the cavity, ν is the frequency of light, V is the volume of the cavity, and c is the speed of light. Using the cavity in Fig. 2, the weighted number of modes is approximated as 2.5.

Let us use this cavity to compare the variance predicted by assuming a uniform spectral distribution of photons in Eq. (1), and the exact results derived in Eq. (14). In Eq. (1) the variance is shown to be:

$$\langle (\Delta n)^2 \rangle \approx \langle n \rangle + \left(.4\right)\langle n \rangle^2 \quad (18)$$

while in Eq. (14) the variance is shown to be (to three significant figures).

$$\langle (\Delta n)^2 \rangle = \langle n \rangle + \left(.459\right)\langle n \rangle^2 \quad (19)$$

The average number of photons in the cavity is about 0.173, found by integrating the spectrum in Fig. 2 and multiplying by the volume of the cavity. The standard uniform spectrum approximation results in about a 1% error in the total variance.

At this point is reasonable to ask if such errors would have a measurable impact on a practical microcavity. A cavity with the spectrum shown in Fig. 2 can be constructed of two Distributed Bragg Reflectors (DBRs) made from alternating SrF_2 and Ge layers, with a doped Ge absorbing layer in a central half-wave cavity layer. The finesse of the cavity is a function of the reflectivity of the mirrors, and absorptivity of the center layer.

Specifically, such a cavity might have a top mirror made of 2 pairs of 528nm thick SrF_2, and 185nm thick Ge layers, followed by an air cavity 571nm thick with a 25nm doped Ge absorbing layer in the center of the cavity, and finally a bottom mirror made from 8 pairs of identical layers as the top mirror.

Two main noise sources, thermomechanical and photon counting noise, can cause the cavity dimensions to depart from their equilibrium positions. Photon pressure within the cavity is another source of noise, although the overall contribution to the total noise is

negligible due the extremely limited number of photons existing in the cavity at any one time. The photon counting noise is inversely proportional to the variance as seen in the following equation [28,29].

$$\langle (\Delta z)^2 \rangle \cong \left(\frac{\lambda}{4\pi F} \right)^2 \frac{1}{\langle (\Delta n)^2 \rangle} \quad (20)$$

In the previous equation λ is the wavelength of light, F is the finesse of the cavity, and z is the displacement of the mirrors and absorber within the cavity relative to their equilibrium positions. If the cavity contains very few photons, the photon counting noise will approach infinity and will dominate all other noise sources. The ambiguity in the cavity center frequency due to the apparent displacement degrades the finesse of the cavity proportionally to the variance in thermal photons. Given a spectrometer with a resolution of $1cm^{-1}$, this cavity could then be used to measure the thermal photon statistics accurately enough to measure a difference between the predictions of equations 18 and 19.

An alternative cavity can be produced where the center frequency is almost independent of the noise, and therefore little or no ambiguity in spectrum occurs. In this case the bottom mirror starts with the Ge layer instead of the SrF_2 layer, and has a total of 10 pairs, also the cavity thickness is increased to 1,135nm. This design is more practical than the previous one where usually a higher finesse is desired. Figure 3 shows the spectral response of the two cavity designs with and without taking into account thermal photon noise.

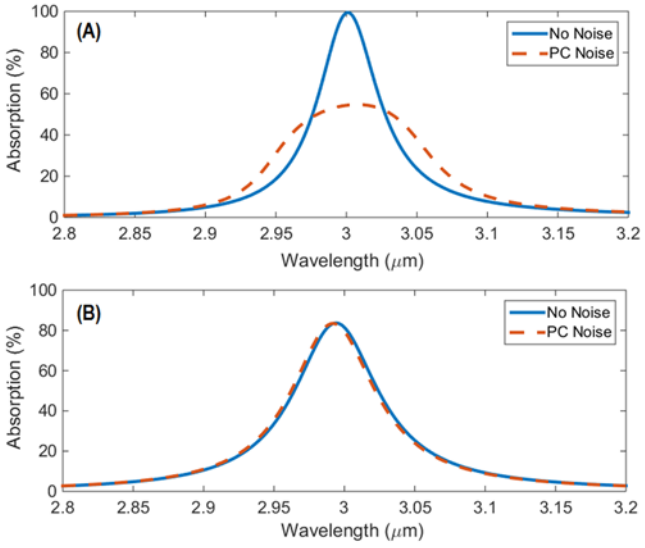

FIG. 3. Photon counting noise limited peak broadening for two cavity designs. The solid lines were calculated for no noise in the system and the dashed lines are calculated from having 50nm of displacement noise in the system. **(A)** The first cavity design showing a dramatic reduction in Finesse as well as peak height. **(B)** The second design where the broadened peak is almost indistinguishable from the peak with no noise broadening.

PART II – Calculating the Noise of Spectrally Selective Thermal Detectors

This section applies the mathematical treatment of Part I to the photon statistics of narrowband or high Q thermal detectors and brings to light the general solution to radiation noise in thermal detectors that do not absorb all wavelengths of radiation with equal efficiency.

INTRODUCTION

For many decades, theory has predicted that Bose-Einstein statistics are a fundamental feature of thermal emission into one or a few optical modes; however, the resulting photon noise has never been experimentally observed. There are at least two reasons for this: 1) relationships to describe the thermal radiation noise for an arbitrary mode structure have yet to be set forth, and 2) the mode and detector constraints necessary for the detection of such light is extremely hard to fulfill. Herein, photon statistics and radiation noise relationships are developed for systems with any number of modes and couplings to an observing space. The results are shown to reproduce existing special cases of thermal emission and are then applied to resonator systems to discuss physically realizable conditions under which Bose-Einstein thermal statistics might be observed. Examples include a single isolated cavity and an emitter cavity coupled to a small detector space. Low mode-number noise theory shows major deviations from solely Bose-Einstein or Poisson treatments and has particular significance because of recent advances in perfect absorption and subwavelength structures both in the long-wave infrared and terahertz regimes. These microresonator devices tend to utilize a small volume with few modes, a regime where the current theory of thermal emission fluctuations and background noise, which was developed decades ago for free space or single-mode cavities, has no derived solutions.

Fundamental treatments of photon noise indicate that thermal emission noise follows Bose-Einstein (BE) statistics rather than Poisson. It is often pointed out that BE behavior is lost or reduced in systems where the thermal emission interacts with many modes, which is a feature of almost every practical implementation. However, even after decades of advances in thermal emitters and photon and thermal detectors, it is still not clear that BE noise for thermal light has ever been observed [30–33]. One difficulty with making such

an observation is that a thermally emitting (or detecting) cavity almost never perfectly couples to just one single mode. Even the highest finesse cavities typically interact with a large number of free-space or external cavity modes, which introduce loss and/or averaging that creates a more Poisson-like statistical behavior. A second difficulty is that systems with few interacting modes are difficult to treat mathematically, and a general solution for thermal statistics in a cavity with an arbitrary mode structure and coupling has only been developed recently. In this paper, we analyze in detail the possibility of observing BE photon statistics in micro-cavities and resonators coupled to free space or other cavities. We develop relationships describing radiation noise for thermal emission or detection systems with any arbitrary mode structure and coupling.

The quantum thermal emission law developed by Planck is one of the pillars of modern physics; however, it must be modified when applied to micro- and nano-systems, where the emitting or absorbing object has a size comparable to or less than that of a wavelength [34,35]. For many devices on this scale, such as detectors, fluctuations are even more important than the base level of the emission, since fluctuations set the ultimate ability of the device to distinguish a signal from the thermal radiation background. The early work on fluctuations [36–42] was performed decades ago on objects and devices interacting with either idealized single modes or the many modes of free space. For the former, photon number fluctuations appear Poissonian for wavelengths near to and shorter than the thermal emission maximum, while they follow BE statistics at very long wavelengths. As discussed above, the presence of many modes averages the BE contribution of each individual mode, resulting in Poisson-like fluctuations.

A fraction of the early work on energy fluctuations and background noise ignored the randomizing nature of many mode systems and contained errors [36,38,40] that have propagated into later treatments and textbooks down to the present day [43–45]. Later treatments of photon statistics and radiation noise [46–48] have handled thermal emission fluctuations for a few additional special cases, most notably that of a system with a number of uniform modes [40,41]. This work pointed discussed the difficulty of a obtaining a general solution for a system with an arbitrary mode structure. Olson, et. al. [49] developed a solution for photon number fluctuations for an idealized arbitrary cavity mode structure, but did not analyze the radiation background noise or the conditions under which BE statistics might be observed.

Despite the progress of these many authors, there remains no general treatment of thermal emission energy fluctuations and radiation noise for objects interacting with an arbitrary mode structure. In previous decades, this was an acceptable situation since nearly

all existing devices interacted with many modes. However, there are currently many structures and devices that have both high spectral selectivity and cavities or volumes comparable to or smaller than λ^3, where λ is the wavelength of light. This combination of properties drives the number of cavity modes downward and makes the relative coupling of each mode to free space (or external cavity) modes of paramount importance. Recent devices with both narrow spectrum and small volume include microresonators [50,51], microcavity detectors [52,53], microcavity emitters and lasers [54,55], perfect absorbers [56,57], and others. Perhaps the most classic example is a narrow spectrum thermal emitter. This is shown conceptually in Fig. 1 coupled to a detector in (a) the same cavity, and (b) an external cavity, to measure the fluctuations. While the physical devices shown in Fig. 1 ostensibly apply to infrared systems, the physical treatment that we discuss applies equally well to terahertz (THz) systems, and the Fabry-Perot cavity in the diagram could be replaced with an appropriate THz resonator. Indeed, BE noise becomes most clearly dominant in the single-mode thermal THz regime. We now turn to an analysis the nature of the radiation background noise that would be observed for a general system.

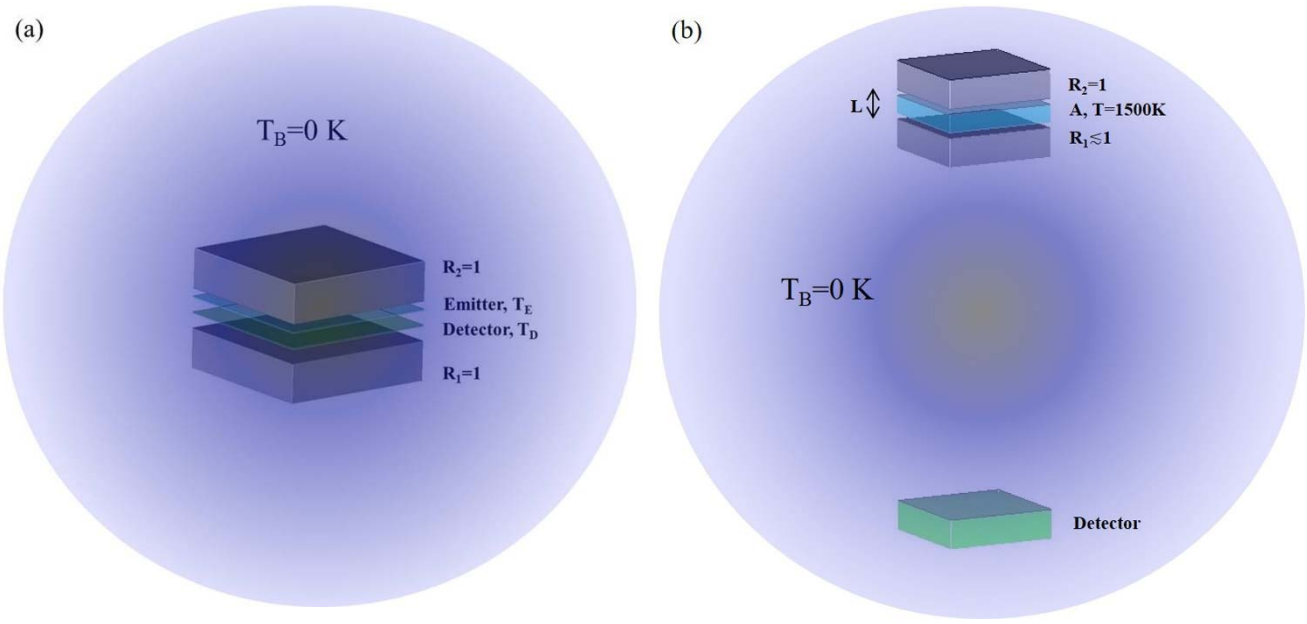

FIG. 1 - Conceptual diagram of a resonator-based thermal emitter that couples to a detector in (a) the same cavity and (b) an external cavity.

DERIVATION AND ANALYSIS OF THERMAL EMISSION ENERGY FLUCTUATIONS WITH A SPECTRALLY DEPENDENT MODE STRUCTURE

Thermal emission energy fluctuations result from time dependent variations in the number of photons emitted from or absorbed by a physical object at a temperature above absolute zero. Over a small frequency range, the square of the thermal emission energy fluctuations of an object can be expressed by multiplying the density of states, square of the photon energy, photon number variance, and volume. For a blackbody in free space, the mode density is $\frac{8\pi\nu^2}{c^3}d\nu$ and the resulting equation is:

$$\left\langle \Delta E^2 \right\rangle = \iint \frac{2\nu^2}{c^3}\left(h\nu\right)^2 \left\langle \Delta n^2 \right\rangle V d\nu d\Omega \qquad (1)$$

where $\left\langle \Delta E^2 \right\rangle$ represents the mean squared energy fluctuation (variance), ν is the photon frequency, c is the speed of light, h is Planck's constant, Ω is solid angle, and $\left\langle \Delta n^2 \right\rangle$ represents the total photon number variance. At this point, the only restriction on

the volume, V, is that it is very large with respect to wavelength. Also note that $\langle \Delta n^2 \rangle$ can be (and is) temperature and frequency dependent.

At very small volumes, where V $\sim \lambda^3$, the distribution of cavity modes deviates substantially from that of free space. The exact mathematical treatment of the mode structure of a microcavity will be highly geometry dependent, but in principle one merely counts the number of modes of the cavity in the spectral range of interest and sums the product of energy squared and photon number variance over each one:

$$\langle \Delta E^2 \rangle = \sum_{\mathrm{m}} (h\nu_m)^2 \langle \Delta n^2 \rangle_{\mathrm{m}} \qquad (2)$$

Since energy fluctuations increase linearly with volume, plots of $\langle \Delta E^2 \rangle$ will usually be normalized by this factor for easier comparison across size scales.

For an object interacting with a single optical mode, the photon number fluctuations satisfy Bose-Einstein statistics [58], such that $\langle \Delta n^2 \rangle_{\mathrm{m}} = \langle n_m \rangle + \langle n_m \rangle^2$, where $\langle n_m \rangle$ is the average photon number in the single mode, m, in the volume of the system. At the opposite extreme is a system with many modes, where thermal emission photons populate the system so that the combined photon statistics become Poisson-like, i.e. $\langle \Delta n^2 \rangle = \langle n \rangle$, where $\langle \Delta n^2 \rangle$ and $\langle n \rangle$ are the photon number variance and average number, respectively, for all modes combined. Between these extremes is the general case of an arbitrary number of modes, most commonly seen in micro- and nano-cavities.

To see how this develops, we note that the average total number of photons must be equal to the sum of the averages for all of the modes, $\langle n \rangle = \sum_m \langle n_m \rangle$. This is true for any general emitter/absorber (not necessarily a blackbody). For thermal emission of a blackbody in equilibrium, we can use the standard equation for the average number of photons in a mode found in many thermodynamics texts [58,59]:

$$\langle n_m \rangle_{BB} = \frac{1}{e^{\frac{h\nu}{kT}} - 1} \qquad (3)$$

If a thermal emitter (or, equivalently, absorber) is not a blackbody, then this equation will be modified by the emissivity, i.e. the coupling strength of the graybody to a specific mode. The expression then becomes:

$$\langle n_m \rangle = \frac{\varepsilon_{\mathrm{m}}}{e^{\frac{h\nu}{kT}} - 1} \qquad (4)$$

or equivalently, $\langle n_m \rangle = \varepsilon_{\mathrm{m}} \langle n_m \rangle_{BB}$. If we use these expressions of photon number in a Bose-Einstein probability distribution, the photon number variance for a system with an arbitrary mode structure takes the form [49],

$$\langle \Delta n^2 \rangle = \langle n \rangle + \frac{\langle n \rangle^2}{M_{eff}} = \sum_m \left(\langle n_m \rangle + \langle n_m \rangle^2 \right) \qquad (5)$$

where

$$\frac{1}{M_{eff}} = \frac{\sum_m \langle n_m \rangle^2}{\left(\sum_m \langle n_m \rangle \right)^2} \qquad (6)$$

Here M_{eff} is the effective number of modes. As one would expect, M_{eff} is a parameter that describes the number of modes interacting with a thermal system, but it differs from the simple mode number because it incorporates different strengths of coupling between the thermal emitter/absorber and each mode. For example, consider the discrete distribution of modes in Figs. 2(a) and 2(b). The first has a uniform set of modes and M_{eff} is obtained merely by counting each one. In Fig. 2(b), the interaction strength of each mode differs from the others. This means that the population of thermally emitted photons into of these modes will be less than predicted from Planck's Law for that frequency and temperature.

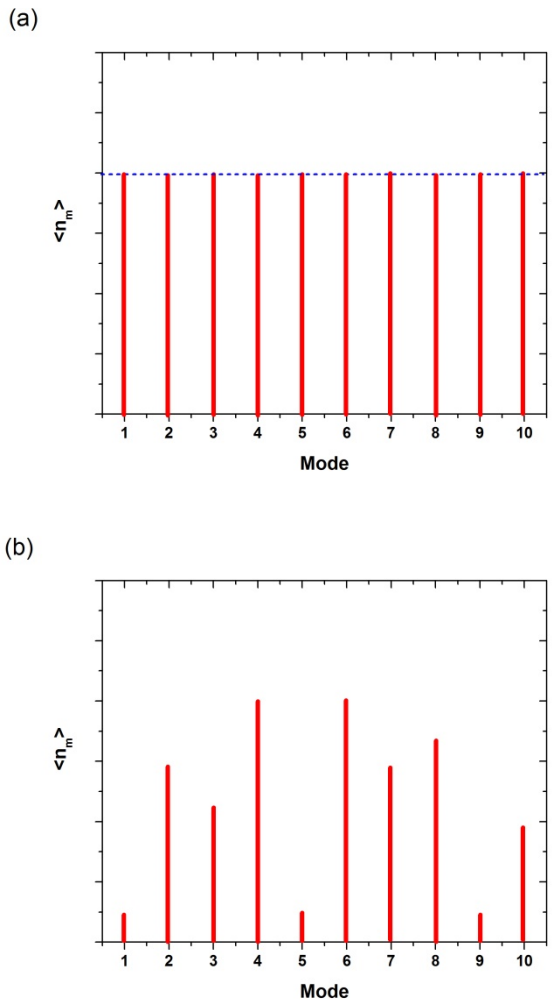

FIG. 2 - Conceptual diagram of a system of modes with (a) uniform (identical) coupling to a thermal emitter, and (b) different couplings for each mode. The effective mode number, M_{eff}, must be calculated for (b) using an average photon number that is weighted by the coupling, or emissivity, of each mode (see Eqns (4) and (6)), or else theory will underestimate the magnitude of BE noise.

We can draw several critical conclusions about thermal emission from this analysis:

1) As stated previously, a single mode system will have Bose-Einstein photon statistics while a many mode system in aggregate will have Poisson. However, *each individual mode of a multiple mode system will have Bose-Einstein statistics, regardless of the system statistics in aggregate.*
2) Any random sample of the photons of a system with Bose Einstein statistics will also have Bose-Einstein statistics. For example, consider a single mode microresonator that

randomly scatters a small fraction of the photons propagating within it out into free space. These scattered photons in aggregate will also have BE statistics (but as will be discussed, a low number density may make the distinction between Poisson and BE statistics difficult to see).

3) Emissivity must be considered per mode prior to the calculation of $\langle \Delta n^2 \rangle$. Often in the literature, one sees photon number fluctuations calculated using a modified Eqn (5), where $\langle \Delta n^2 \rangle$ for a blackbody is directly multiplied by $\varepsilon(\nu,\Omega)$, but this calculation is not correct. Granted, it has negligible errors at wavelengths equal to or shorter than the peak thermal emission wavelength, but it can have significant errors for individual (or few) modes at wavelengths significantly longer than the thermal emission peak. The proper expression is:

$$\begin{aligned} \langle \Delta n^2 \rangle &= \sum_{\mathrm{m}} \langle n_m \rangle + \langle n_m \rangle^2 \\ &= \sum_{\mathrm{m}} \left[\frac{\varepsilon_m}{e^{\frac{h\nu}{kT}} - 1} + \left(\frac{\varepsilon_m}{e^{\frac{h\nu}{kT}} - 1} \right)^2 \right] \end{aligned} \qquad (7)$$

4) The frequency spacing between modes does not affect the photon number fluctuations except through the emissivity (i.e. coupling) of each mode and the natural frequency dependence of Planck's Law. In other words, two modes separated by 1nm in wavelength would have the same number fluctuations as two separated by 2nm unless the emissivity or population significantly changed over that wavelength range.
5) The Bose-Einstein statistics of a single mode of a many mode system may be difficult to distinguish from Poisson statistics. First, the spectral resolution necessary to see a single mode is extremely high. Second, since $\langle n_m \rangle$ is only a small fraction of $\langle n \rangle$, the magnitude of the $\langle n_m \rangle^2$ term will be extremely small compared to $\langle n \rangle^2$. This is particularly true for common visible wavelength ranges, where the average population of photons in a mode as given by Eqn (4) is much less than 1 and distinguishing $\langle n_m \rangle + \langle n_m \rangle^2$ from $\langle n_m \rangle$ could be impractical. Conversely, a few mode system

working at long wavelengths and elevated temperatures could allow Bose Einstein statistics to be seen by sampling a fraction of the spectral range of the overall thermal system.

6) The numbers of modes are not determined solely by the isolated detector or emitter volumes (if they are separated into different cavities), but rather by the total mode structure of the coupled emitter-detector system. For example, a heated single mode cavity emitting toward a detector in free space would not be single mode for purposes of photon statistics and radiation noise since multiple free space modes will couple with the emitting cavity mode.

OBSERVING BOSE-EINSTEIN STATISTICS IN THERMAL EMISSION

From the previous discussion, it is clear that only thermal systems with a single mode or few modes will ever be observed to have Bose-Einstein statistics. This condition is usually extremely difficult to produce in practice. Recall the simple case of a spectrally narrow heated device emitting into free space, where the radiation noise is measured by an ideal detector. The number of modes in a spectral region in free space is given by $\frac{8\pi v^2 V}{c^3} dv$. For a typical-size laboratory, where $V = (3m)^3$, and an emission wavelength and frequency of $\lambda = 5\mu m$ and 60THz, respectively, the spectral resolution of an emitting cavity would have to be narrower than about 2.3×10^{-5} Hz in order for the emitted photons to be confined to a single free space mode. This corresponds to a microcavity finesse on the order of or exceeding 10^{18}, which is many orders of magnitude beyond experimentally achievable values [60–62].

Therefore, in order to have few modes, not only must the emitter be confined to a small volume, but the detector interactions with its enclosing volume, whether large or small, must be considered as well. The emitter and detector can either be confined to the same cavity (volume), or they can be separated into two coupled volumes. We will consider each case in turn below.

Observing Bose Einstein radiation background noise within a single cavity

A single cavity containing an emitter and detector was shown in Fig. 1(a). The diagram is of an infrared Fabry-Perot cavity, but for generality, it could be replaced with a THz resonator also containing a detector and emitter. This cavity is ideal, one-dimensional, and

lossless, having mirrors of 100% reflectivity, and the space in which it resides has perfectly absorbing walls and is held at absolute zero. This space can have any volume but to place a lower bound on the observability of BE noise, it will be considered infinitely large. Smaller volumes will confine the lateral dimensions and, because of the smaller mode density with create fewer interactions with non-cavity axis modes. With perfectly reflective mirrors, the finesse of the cavity is defined by the absorption of the emitter and detector. The detector and emitter have been placed between the two mirrors, for example, each at a different intensity peak in the standing wave patterns within the cavity for maximum coupling. Other positions within the cavity or as part of the mirrors are possible with appropriate adjustments of the coupling calculations. It is important to note that the cavity system may have many modes in total; however, the emitter and detector will interact most strongly through the cavity modes defined along the cavity axis because radiation emitted in other directions will be immediately absorbed by the walls of the already-mentioned enclosing space held at absolute zero.

Let the emitter have a single-pass absorption, A/2, and a temperature T_E and the detector have the same absorption but temperature, T_D. The finesse of this cavity can be calculated[63] to be $F = \frac{\pi\sqrt{1-A}}{A}$. (Note that equal absorptions are merely a simplification and not a necessary condition for the analysis below.) In order to best identify energy fluctuations of the emitter, the detector temperature must be low, assisted by cryogenically cooling the entire cavity system to near absolute zero. The emitter temperature must be raised to a high value by, say, joule or inductive heating. We note that in reality for a fully confined, lossless cavity, it would be impossible to raise the emitter temperature by external means because no connection to the outside world would be allowed; however, for purposes of this example we will assume that heating takes place, for example, inductively via a frequency far from the resonance or via joule heating with wires aligned away from the cavity axis, so that the system can be considered lossless along the cavity axis over the (narrow) spectral absorption range of the detector.

Some sort of external attachment to the detector is also necessary for both the logical reason that there must be some means to hold it in place and read out the signal and the fundamental reason that the detector must be cooled because in a system solely limited by radiation heat transfer, radiation coupling along the cavity axis will raise the temperature of the detector to levels that would make seeing the energy fluctuations of a single emitter mode impossible. Let us examine this latter point in more detail.

The temperatures T_E and T_D are not independent because they are coupled via thermal

radiation emitted within the cavity resonance, and the detector must absorb light of this frequency and direction or else the noise characteristics cannot be determined. If the cavity heat transfer is completely radiation-limited, the temperature of the detector can be written as a function of the background and emitter temperatures as:

$$\sum_{\mathrm{m}} \frac{\varepsilon_{ED} h\nu}{e^{\frac{h\nu}{kT_E}} - 1} + \int_0^\infty \int_{\Omega_{space}} \frac{2\nu^2}{c^3} \frac{\varepsilon_D h\nu}{e^{\frac{h\nu}{kT_B}} - 1} d\Omega d\nu$$
$$= \sum_{\mathrm{m}} \frac{\varepsilon_{ED} h\nu}{e^{\frac{h\nu}{kT_D}} - 1} + \int_0^\infty \int_{\Omega_{space}} \frac{2\nu^2}{c^3} \frac{\varepsilon_D h\nu}{e^{\frac{h\nu}{kT_D}} - 1} d\Omega d\nu \qquad (8)$$

where T_B is the background temperature, probably 0K, ε_D is the emissivity of the detector into free space which can be a function of ν and Ω, ε_{ED} is the coupling between emitter and detector in the cavity, and Ω_{space} represents the solid angle distribution of detector emission outside the cavity, (i.e. $4\pi - \Omega_{cav}$, where Ω_{cav} represents the solid angle distribution of the cavity modes). Note that we do not need to include the emitter fluctuations to the background in the equation because it is only the detector that is observing the fluctuations, so only interactions that couple directly to the detector are relevant. See Fig. 3 for a conceptual diagram of the cavity geometry. The first term on the left hand side represents the energy emitted from the emitter to detector, the second term on the left side represents the energy emitted from the background to the detector, the first term on the right represents the energy emitted from detector to emitter, and the second term on the right side represents the emission from detector to background. Of these terms, the emission from detector to emitter ($T_D << T_E$) and the emission from the background ($T_B \sim 0K$) to the detector can be neglected in an idealized analysis, in which case we can rewrite the above as:

$$\sum_{\mathrm{m}} \frac{\varepsilon_{ED} h\nu}{e^{\frac{h\nu}{kT_E}} - 1} = \int_0^\infty \int_{\Omega_{space}} \frac{2\nu^2}{c^3} \frac{\varepsilon_D h\nu}{e^{\frac{h\nu}{kT_D}} - 1} d\Omega d\nu \qquad (9)$$

We have assumed that the volume surrounding the open-sided cavity is large enough to be considered free space. This is not a necessary condition, but it does allow us to maximize the peripheral mode number and therefore minimize the equilibrium detector temperature

in a radiation-limited system.

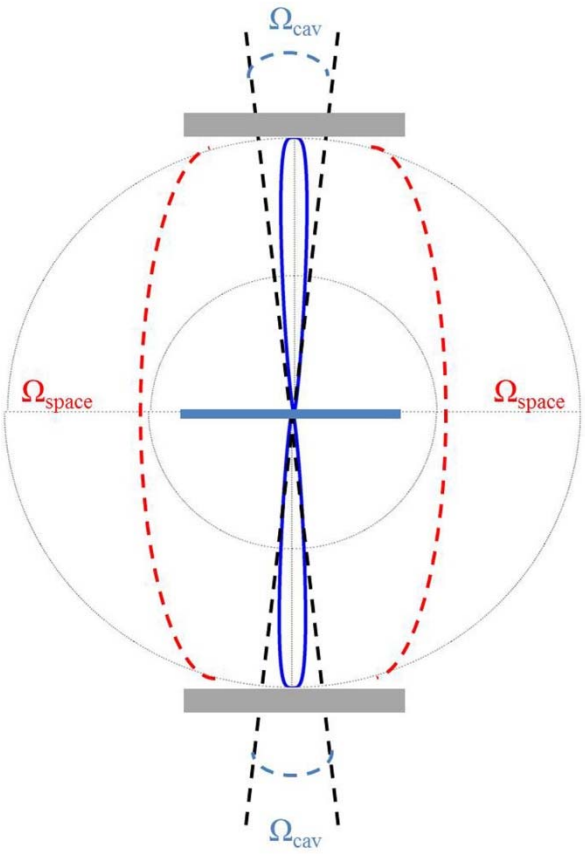

FIG. 3 - Diagram of the solid angles used in noise and radiation heat transfer calculations of a single cavity containing a coupled emitter and detector.

From the above equation, if we select a temperature, T_E, for the emitter, say by introducing a joule heating current into the emitter plate, then we can calculate the steady-state detector temperature. Once we have determined this, we can estimate the energy fluctuations and radiation noise of the system. The detector will have two dominant sources of radiation noise: absorbed radiation from the emitter via the fundamental cavity mode, and emitted radiation from the detector itself due to its finite temperature, T_D. This latter noise is emitted to all available modes, not merely those aligned along the cavity axis, and since the number of peripheral modes can be very high, they will usually dominate the detector emission fluctuations. In order to measure only the radiation noise in the few (or one) modes along the cavity axis, the emitter radiation fluctuations must greatly exceed the detector emitted fluctuations, $\left\langle \Delta E^2 \right\rangle_{emitter} >> \left\langle \Delta E^2 \right\rangle_{detector}$. Calculating this condition

involves integrating the energy fluctuations for the detector (right hand side) over all modes and space and then solving for T_D for a given T_E such that this is much less than the energy fluctuations of the emitter (left hand side) in the relevant cavity mode(s):

$$\sum_{\mathrm{m}} (h\nu)^2 \left[\frac{\varepsilon_{ED}}{e^{\frac{h\nu}{kT}} - 1} + \left(\frac{\varepsilon_{ED}}{e^{\frac{h\nu}{kT}} - 1} \right)^2 \right]_{\mathrm{m}} \\ >> \int \int_{\Omega_{space}} \frac{2\nu^2}{c^3} (h\nu)^2 \left[\frac{\varepsilon_D}{e^{\frac{h\nu}{kT}} - 1} + \left(\frac{\varepsilon_D}{e^{\frac{h\nu}{kT}} - 1} \right)^2 \right] V d\Omega d\nu \tag{10}$$

In the above expression, we have again neglected the background emission everywhere and detector emission in the main cavity modes because any practical solution to the above condition will require T_B to be small and $T_E >> T_D$; therefore, the detector fluctuations in the cavity and the background fluctuations elsewhere will be negligible. Note that the above expression is a conservative estimate for measurability because we have assumed that any emission outside the main cavity axis occurs into free space; emission into a more limited volume will involve a smaller mode density and thus a smaller contribution to energy fluctuations, improving our prospects of detecting Bose-Einstein noise.

In Fig. 4, we show solutions for Eqns (9) and (10) for a single mode half-wave cavity at various resonance wavelengths, using the condition that the "much greater than" symbol refers to exactly one order of magnitude. In this plot, we have changed the emitter temperature, T_E, in the single mode cavity by, for example, introducing a controlled current to induce joule heating. The detector temperature is forced to a finite value by radiation transfer from the emitter. For simplicity, the background has been assumed to be at T=0K. At this point, we know the temperature of both the emitter and detector for purely radiation-limited heat transfer. We can now calculate from the maximum detector temperature that will allow the radiation background noise measured by the detector to be dominated by received radiation from the emitter, as predicted by Eqn (10). Domination by the emitter is crucial since, at a given wavelength, higher temperature objects will have a stronger BE component to their photon statistics and the emitter-detector coupling only covers one or a small number of modes, making BE statistics observable. From this data, we can see that at almost all elevated temperatures, *the maximum acceptable detector temperature is lower than can be achieved in a radiation-limited system, which means that we must have some*

degree of detector cooling via heat conduction. Note that this conclusion is relatively independent of cavity finesse.

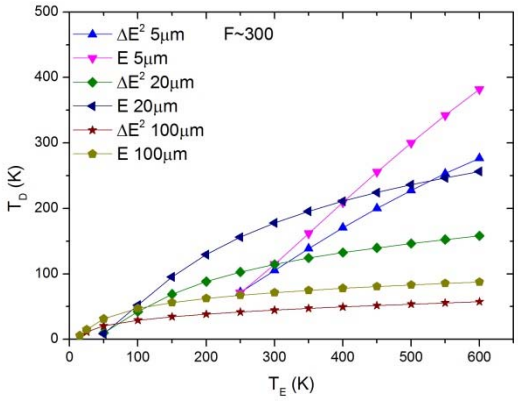

FIG. 4 - Plots of **(E)** the detector temperature versus emitter temperature for a single isolated cavity and **(ΔE^2)** the maximum detector temperature such that overall detector energy fluctuations are dominated by received power from the emitter (an order of magnitude greater than other sources). When the emitter is heated, it gives off radiation, some of which is absorbed by the detector. This raises the temperature of the detector to an equilibrium temperature, T_D. The detector then has a radiation noise with contributions from fluctuations in the received emitter energy and the fluctuations of its own emitted energy. To observe BE noise, the former should dominate, and in these plots, that is not the case if radiation heat transfer is the only mechanism determining T_D. Some external cooling mechanism must be used to meet the condition of Eqn (10). The curves are solutions for Eqns. (9) and (10) for a single mode half-wave cavity at various resonance wavelengths with A_E=0.005 and A_D=0.005. The cavity can be considered as similar to that in Fig. 1(a).

Figures 6-9 quantify the radiation background fluctuations for a single cavity system as a function of emitter temperature, finesse, cavity resonant wavelength, and number of longitudinal modes. In each case, the actual energy fluctuations are compared to the case of a perfect Poisson system and an extreme BE system (where $\left\langle \Delta n^2 \right\rangle \sim \left\langle n \right\rangle^2$). The data above establishes that, for a cavity with total isolation in one dimension, the primary criteria for observability for BE background noise in a single cavity are 1) a high emitter temperature, 2) an extremely long observation wavelength, and 3) a sufficiently low detector temperature relative to the emitter.

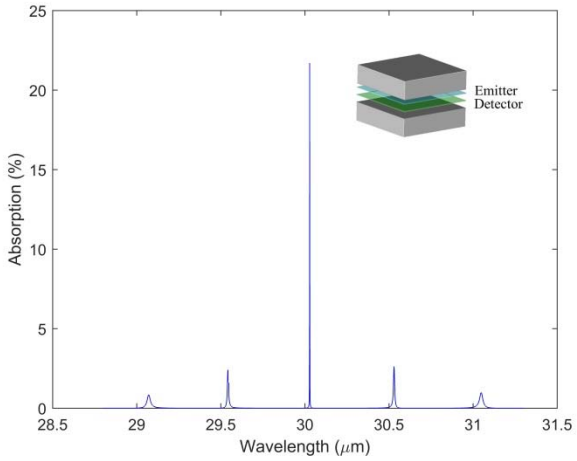

FIG. 5 - Conceptual diagram of the modes of a single cavity containing an emitter and detector of the type shown in Fig. 1 (a). The simulations of Figs. 6-9 are based on variations around this basic cavity. TABLE I describes the layer structure in detail. The layers include 5.5 pairs of $3\mu m$ n=2.5 and $6\mu m$ n=1.25, $135\mu m$ n=1, 60nm n=2-2i, $750\mu m$ n=1 (A), another 60nm n=2-2i, $15.75\mu m$ n=1, and 9.5 pairs of $3\mu m$ n=2.5 and 6μm n=1.25.

TABLE I. Layer structure for the 5-mode single cavity of Fig. 5 at $30\mu m$.

	Thickness (μm)	Index	
5.5 pairs	3/6	2.5/1.25	
1	135	1	
1	0.06	2-2i	Detector
1	750	1	A
1	0.06	2-2i	Emitter
1	15.75	1	
9.5 pairs	3/6	2.5/1.25	

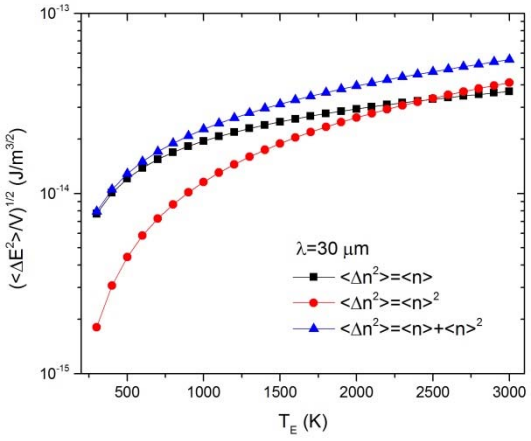

FIG. 6 - Radiation background fluctuations as a function of emitter temperature for an isolated single cavity containing an emitter and detector. The plots for <n> and <n>^{2} are merely to show the relative importance of each term in the overall noise of the system, which is based on <n> + <n>^{2}. TABLE I describes the layer structure. Also, adjust length of A in TABLE I to obtain $n\lambda/2$ and volume.

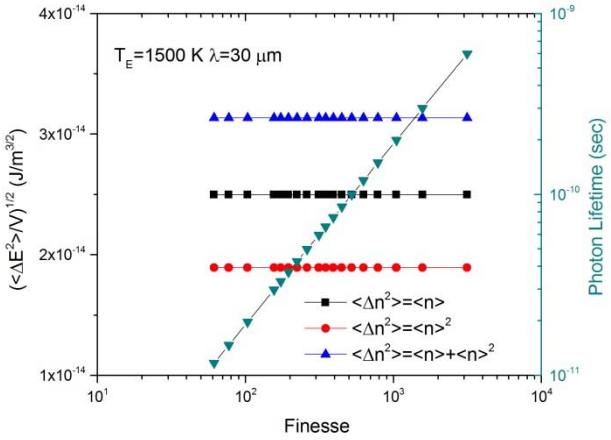

FIG. 7 - Radiation background fluctuations as a function of finesse for an isolated single-mode cavity containing an emitter and detector. Since there is only one mode regardless of spectral width and the detector is at a low enough temperature that it does not emit significant radiation to the peripheral background, the fluctuations are constant. The plots for <n> and <n>^{2} are merely to show the relative importance of each term in the overall noise of the system, which is based on <n> + <n>^{2}. TABLE I describes the layer structure. Also, adjust length of A in TABLE I to obtain $n\lambda/2$ and volume.

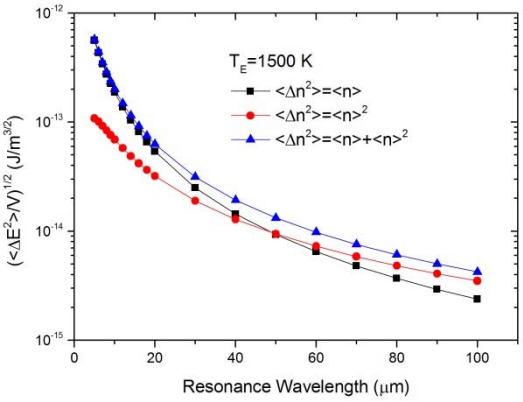

FIG. 8 - Radiation background fluctuations for a single cavity system as a function of cavity resonant wavelength. Note that the actual fluctuations (<n> + <n>^{2}) are indistinguishable from Poisson statistics for wavelengths less than about $10\mu m$ and only become clearly differentiated above $20\mu m$. TABLE I describes the layer structure. Also, adjust length of A in TABLE I to obtain $n\lambda/2$ and volume.

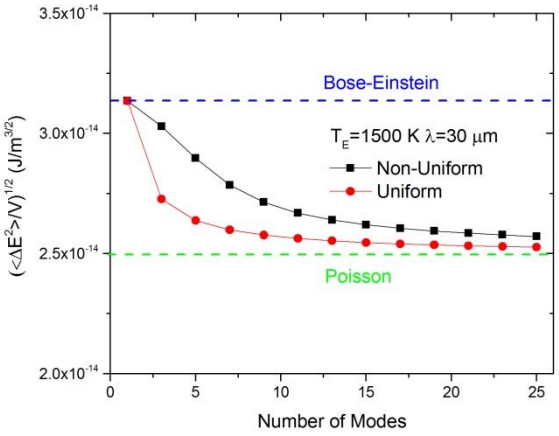

FIG. 9 - Radiation background fluctuations for a single cavity system as a function of longitudinal modes. In this plot, we have taken the same cavity system from Figs. 6-8, except that the length has been increased to introduce additional modes into the detector absorption pass band. The "Non-Uniform" curve represents the data of interest, while "Uniform" curve refers to a hypothetical system where all modes couple equally to the emitter and is included for comparison. TABLE I describes the layer structure. Also, adjust length of A in TABLE I to obtain $n\lambda/2$ and volume.

Interestingly, cavity finesse is essentially irrelevant in the case of the isolated resonator because the average number of photons is determined by the number of modes, not the spectral width of any mode resonance. Spectral width is only involved when there is another space with modes with which the cavity could couple. However, cavity finesses play a very important role in determining the photon lifetime of a system. This is important because any fluctuation in the mode energy is by its nature very transient. A deviation of the number of photons from average will exist on average for only a photon lifetime. This means that any detector hoping to see these fluctuations must operate with a response time on the order of the photon lifetime or faster. Otherwise, the noise will be observed as an average over many photon lifetimes, which will revert the statistics to Poissonian. Additional discussion of detectors will be delayed to later.

We note that the wavelength needed to observe BE noise is longer than would be expected from a simple calculation using Eqn (3). Instead, Eqn (4) must be used because of the imperfect coupling between the emitter and detector, ε_{ED}. The required long wavelengths make the isolated single cavity case most compatible with a THz resonator, although differences between Poisson and BE will be visible in the long-wavelength infrared as well.

One additional question that deserves discussion is whether it would be possible to see BE noise using outcoupled light from a high finesse resonator via a coupled waveguide or scattering defect without the need to include a detector inside the resonator. This is definitely possible, but will run into the issue raised in conclusion 2 from our thermal emission discussion earlier in the paper. As one samples a photon population, one is reducing the number of observed photons to well below the actual number in a mode. Since the BE component of noise relies on $\langle n \rangle^2$, our ability to distinguish BE from Poisson becomes much more difficult. On the other hand, a large sample cannot be outcoupled (at least in steady-state) from the primary resonator mode because this loss will then limit the isolation of the resonator, causing it to interact more strongly with the modes of the environment. Truly a conundrum!

Another issue with waveguide outcoupling is that an extremely long length waveguide introduces many modes onto the propagation axis, while a shorter waveguide develops tunneling modes as the length decreases, eventually approaching near-free-space densities as the length becomes very short.

Observing Bose Einstein radiation background noise in coupled spaces

It is also possible to observe BE noise in two coupled cavities as we will now argue. Consider, the configuration of Fig. 1(b). Here a single mode cavity containing a heated emitter is coupled to an external observing space containing a cryogenically cooled detector. This detector will be assumed to cold shielded and filtered so that it is only responsive to the spectral emission of the fundamental mode of the emitter cavity. The detector cavity will contain many modes, the number of which will be determined by the size of the cavity, which is a variable that we will control. For simplicity, we will assume a cavity that has lateral dimensions of $\lambda/2$ by $\lambda/2$, but with a length of $n\lambda/2$, where n is an integer that we can control to alter the volume of the cavity. In this system, the walls of the detector cavity have perfect reflectivity, $R_d=1$, but the detector itself has an absorption and is positioned as shown in the inset of Fig. 10 and described in TABLE II. The emitter cavity has a perfectly reflecting back mirror, $R_b = 1$, but a front mirror, that is, the mirror that couples the emitter and detector cavities, that has a reflectivity, $R_f < 1$. In this way, the two cavities are coupled to one another but completely isolated from the outside world. The single mode version of this coupled cavity system has a photon lifetime of 0.14ns.

The volume (determined by length in our specific example) of the detector plays a dominant role in how many modes interact with the emitted photons and thus the amount of BE behavior that will be seen in the noise. However, R_f and the absorptions of the detector and emitter also have a large effect since they help determine the width of the resonances within the emission envelope, as shown in Fig. 10. In this figure, a system is shown where approximately five detector cavity modes couple at some level with the emitter resonance. In Fig. 10, the resonances are shown as extremely narrow, but these would widen if the single-pass absorption of the detector, A_d, could be hypothetically increased without affecting the other parameters of the cavity. This concept is shown in Fig. 11. As A_d increases, coherent interactions decrease, and the resonances widen. In the case of extremely high detector absorption, where A_d approaches 1, the width of the resonances that originate with the detector widen towards infinity and the coupling peak-to-valley difference (frequency dependence of coupling) decreases as the valley minimums move towards perfect absorption. This effectively creates a uniform mode structure in the cavity system. When the detector resonances are very narrow compared to the emitter resonance, each mode couples differently, and we must turn to the effective mode calculation discussed previously in order to calculate the noise fluctuations, as shown in Fig. 12. Figure 13 shows the noise fluctuations as a function of cavity volume for the ideal cases of Poisson

statistics, BE statistics, and uniform modes, and the actual case of coupled modes. Figure 13 shows the plot for T_E = 1500K at $\lambda = 50\mu m$. As with the single cavity case, we can see that distinguishing BE from Poisson statistics is still difficult at short infrared wavelengths. At $5\mu m$, a difference of less than 3% is seen in a single mode system. At longer infrared wavelengths, however, as shown in Fig. 13, and into the THz range, the distinction between BE and Poisson is very clear if a single or few mode system can be created.

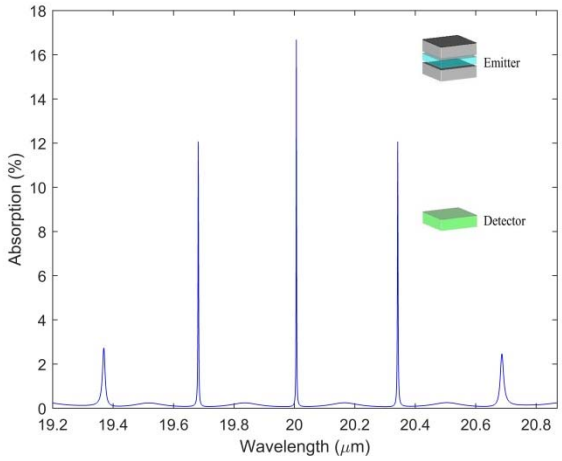

FIG. 10 - Conceptual diagram of the modes of two coupled cavities as shown in the inset. The short cavity contains the emitter at elevated temperature and the second cavity the detector. The photon lifetime of this coupled cavity system is 0.14ns. TABLE II describes the layer structure in detail. The layers include 4.5 pairs of $2\mu m$ n=2.5 and $4\mu m$ n=1.25, $600\mu m$ n=1 (A), 40nm n=2-2i, another $600\mu m$ n=1 (B), 2.5 pairs of $2\mu m$ n=2.5 and $4\mu m$ n=1.25, $8\mu m$ n=1.25, 1.5 pairs of $2\mu m$ n=2.5 and $4\mu m$ n=1.25, $5\mu m$ n=1, 20 nm n=2-2i, another $5\mu m$ n=1, and 9.5 pairs of $2\mu m$ n=2.5 and $4\mu m$ n=1.25.

TABLE II. Layer structure for the 5-mode coupled cavity at $20\mu m$.

	Thickness (μm)	Index	
4.5 pairs	2/4	2.5/1.25	
1	600	1	A
1	0.4	2-2i	Detector
1	600	1	B
2.5 pairs	2/4	2.5/1.25	
1	8	1.25	
1.5 pairs	2/4	2.5/1.25	
1	5	1	

1	0.02	2-2i	Emitter
1	5	1	
9.5 pairs	2/4	2.5/1.25	

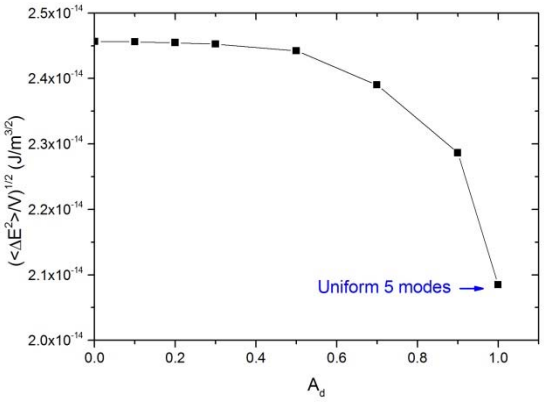

FIG. 11 - Plot of energy fluctuations versus detector absorption for a basic coupled-cavity system in the case where 5 modes have been coupled to the detector. The emitter cavity parameters are: R_1=0.999, R_2=1, A=0.001, $L = 10\mu m$, and T=1500K. As the detector absorption increases, the coupled resonances become broader, effectively becoming uniform as A_d approaches one.

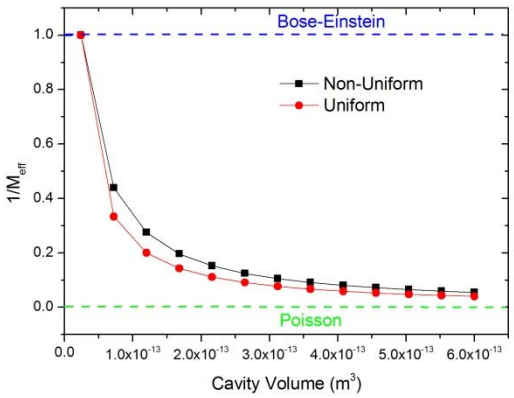

FIG. 12 - Plot of inverse effective mode number versus cavity volume for the basic coupled cavity of Fig.10. For comparison, plots of a perfect BE system (M = M_{eff} = 1), a perfect Poisson system (M = M_{eff} = ∞), and a uniform mode system (M_{eff} = M) have been made. TABLE II describes the layer structure. Also, adjust length of A and B in TABLE II to obtain $n\lambda/2$ and volume.

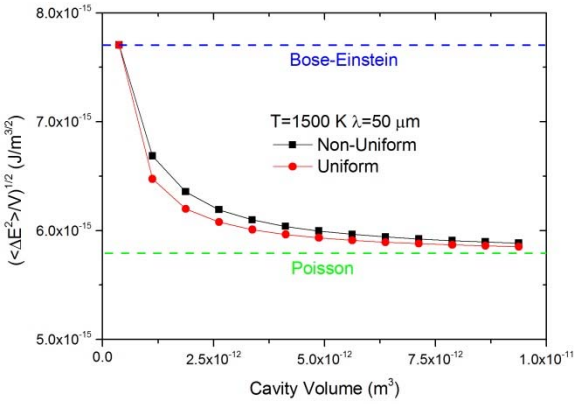

FIG. 13 - Energy fluctuations versus cavity volume for a coupled cavity system with the basic structure of Fig. 10 for a center wavelength of $50\mu m$. For comparison, plots of a perfect BE system (M = M_{eff} = 1), a perfect Poisson system (M = $M_{eff} = \infty$), and a uniform mode system (M_{eff} = M) have been made. TABLE II describes the layer structure. Also, adjust length of A and B in TABLE II to obtain $n\lambda/2$ and volume.

Before concluding, it is useful to speculate on the chances of observing Bose-Einstein statistics in thermal emission. This analysis has shown that such observation is possible in theory. The magnitudes of the differences between Poisson and BE noise become quite significant under the right conditions. However, there are significant practical difficulties. The first involves the spectral regime. BE noise will only dominate over Poisson noise for emitters at elevated temperatures and systems operating at long wavelengths. For example, this paper used $\lambda \sim 30\mu m$ and T_E = 1500K, and ranges with temperatures and wavelengths scaled appropriately or higher/longer are viable. Interestingly, the finesse requirements of cavities or resonators are not a major factor in the success or failure of BE noise detection. Unfortunately, though, the materials and device technologies for the above wavelength ranges are not nearly as advanced as in the visible and near-IR. There are few materials that could be fabricated into modally isolated far-IR cavities. Possibilities include diamond and ionic solids such as KBr, but significant technological development would be necessary to create low-loss high reflectivity coatings and resonators. Metallic or metamaterial resonators in the THz perhaps provide a better path forward as they can be isolated from external world by the metal of the resonator itself. Small metallic losses within the resonator are acceptable for mode coupling as the finesse needs to be high enough to ensure that the coupling of the system is dominated by the emitter and detector, but not so high that finesses typical of near-IR microresonators are necessary. However,

there are significant photon lifetime issues introduced by the finesse. As mentioned previously, any detector must be able to sample the photon number of the system with a response lifetime comparable to or faster than the photon lifetime. Although the photon lifetime varies wildly depending on the cavity design, a value on the order of 100ps is a reasonable working number. At infrared frequencies, the number of photons in a mode dominated by BE statistics will be slightly greater than one. (There may be several or more photons on average for a mode in the THz.) This means that detectors must be able to distinguish individual photons in the infrared at speeds compatible with the photon lifetime. This would be a difficult task even for cryogenically cooled telecommunications-grade technology; in the far-infrared and THz, such detector technology is not currently available.

PART III: High-Q Diamond Microresonators in the Long-Wave Infrared

This report section discusses our successful efforts to develop high Q LWIR microresonators in support of Goal 2.

Executive Summary:
High Q photonic devices in the room temperature thermal infrared region, corresponding to wavelengths between 8 and 12 microns, have been demonstrated for the first time. Whispering gallery mode diamond microresonators were fabricated using single crystal diamond substrates and oxygen plasma inductively coupled plasma (ICP) reactive ion etching (RIE) at high angles. The spectral characteristics of the devices were probed at room temperature using a tunable quantum cascade laser that was free space-coupled into the resonators. Light was extracted via an arsenic selenide chalcogenide infrared fiber and directed to a cryogenically cooled HgCdTe detector. The quality factors were tested in multiple microresonators across a wide spectral range from 9 to 9.7 micron with similar performance. One example resonance (of many comparables) was found to reach 3648 at 9.601μm. Fourier analysis of the many resonances of each device showed free spectral ranges slightly greater than 40GHz, matching theoretical expectations for the microresonator diameter and the overlap of the whispering gallery mode with the diamond.

Introduction

The quality factors of cavities and microresonators have reached astounding levels in many regions of the spectrum from the ultraviolet to the infrared, with Q reaching values of hundreds of thousands or higher. Ready examples are aluminum nitride (AlN) microring resonators with quality factors near 10^5 at 390nm in the UV [64], paraffin or silicone oil droplets with quality factors of near 10^7 at 640nm in the visible [66], silicon microtoroids with quality factors above 10^8 near 1.55μm in the near-infrared [71], and fluoride microdisks with quality factors near 10^8 at 4.4μm in the mid-wave infrared [84]. Further, the above works represent only a fraction of many other outstanding devices that illustrate high Q in many regions of the spectrum [64-86].

In the thermal infrared and beyond, however, the demonstrated quality factors of cavities and resonators have been much lower, barely reaching 50 in most reported work [87-91]. Much of the difficulty in reaching high Q at long wavelengths lies with the high absorptions of even the most transparent materials. One of the most technologically

important infrared regions lies between wavelengths of 8μm and 12μm, near the peak energy density of room temperature thermal emission. We will note that the wavelength ranges between 8-12μm or 8-14μm are often called the long-wave infrared (LWIR) in engineering parlance, although the definition of what constitutes mid-wave and long-wave infrared varies considerably in different fields such as astronomy, and we merely use this definition for consistency with our measurement cameras and detectors. In this region of the spectrum, chemically stable materials such as germanium and zinc selenide are often used as optical elements, but their absorptions are only low enough to support single-pass optical propagation or a few passes at most. High Q resonators require extreme transparency so that the effective optical propagation length within the cavity or resonator is compatible with long coherence lengths.

Figure 1 shows a plot of absorption versus wavelength for a number of common infrared materials. In this plot a dotted line is shown that corresponds to the maximum absorption that would allow a Q on the order of 10^5, which is a level that is unremarkable at shorter wavelengths but far above currently achievable values in the LWIR. Unfortunately, there are very few materials that meet the appropriate absorption criteria. There are several types of ionic salts, such as KBr, that have very low absorption in the thermal infrared; however, these materials dissolve in water and are chemically unstable in many fabrication processes and non-laboratory end-user environments.

The other possible choice is diamond. Diamond has a series of strong multiphonon absorption peaks extending from roughly 3 to 6μm in the infrared, but beyond these wavelengths in its pure state, it has no other major solid-state vibrational states that can interact with thermal infrared light. Therefore, in theory the Q of a diamond microresonator would be limited by impurity absorption, or more likely, scattering due to fabrication imperfections. The fabrication technology for diamond is still in its early stages, but significant progress is being made [93-101] to increase the types of fabrication processes in which diamond can be used and, perhaps most critically for microresonators, to reduce the surface roughness caused by etching and patterning. With these advances, whispering-gallery mode resonators of diamond have been demonstrated with high optical quality factors at short wavelengths [93,94,99-103].

In this paper, diamond microdisks were fabricated from single crystal substrates and oxygen-based ICP RIE at high angles. LWIR light from a tunable quantum cascade laser emitting from $\lambda \sim 9.0\mu m$ to $9.7\mu m$ was introduced into the microresonator whispering gallery modes via free-space coupling, and out-coupling was performed with an arsenic selenide fiber that guided the light to a cryogenically cooled HgCdTe detector. The

microresonator and the rest of the laboratory environment was at room temperature. The measured quality factors for two specific wavelengths on two separate samples were found to be 3648 at 9.601μm and 3130 at 9.541μm respectively. However, many resonances were measured with comparable performance. A Fourier analysis of the resonances as a whole showed that the free spectral ranges of the microdisks were slightly greater than 40GHz which matches our theoretical predictions based on the microresonator diameter and the whispering gallery mode overlap with the diamond.

Fabrication of Single-Crystal Diamond Microdisks

Figure 2 shows the fabrication process flow. Microdisks were patterned from CVD single-crystal diamond plates ($3mm \times 3mm \times 250\mu m$, Element Six). Before processing, the single-crystal diamond plates were cleaned in a set of boiling acids and bases for few minutes. Specifically a sequence of RCA1, RCA2, and piranha solutions were used. The substrates were rinsed in deionized water for few minutes between etch step. After cleaning, silicon nitride was deposited in a high density plasma chemical vapor deposition (HDPCVD) process and used as a hard mask. After standard photolithography, inductively coupled plasma reactive ion etching (ICP RIE) was used to pattern the silicon nitride and etch the diamond. The etch rate of the diamond was approximately 150 nm/min with conditions of 30 sccm oxygen flow, 100 mW RF power, 700 W ICP power, and a 5 mtorr background pressure. Next, an additional layer of silicon nitride was deposited over both the microresonator disk and the substrate. Another ICP RIE step removed the substrate portion of the nitride, but leaving nitride on the disk. Since ICP RIE is a high aspect-ratio process, we designed the etch to leave substantial material on the resonator disk sidewalls. This step is shown from Figure 2e to Figure 2f. The sidewall silicon nitride surrounding formed a protective layer that prevented it from attack during subsequent processing.

After this, another ICP RIE process etched the diamond to produce the desired height of the microdisks. This height was chosen both for ease of processing and to ensure that whispering gallery mode coupling to the substrate would be minimal. The diamond substrates were then mounted vertically and an angled ICP RIE etch undercut the microdisks to create the propagation ring of the resonator. Finally, the rest of protective silicon nitride was removed using a buffered oxide etch (BOE).

Figures 3a and 3b are the images taken by scanning electron microscope (SEM) when sample was tilted at 75 degrees. The undercut can be observed at the edge of diamond microdisk in Figure 3a. Figure 3b is a close-up of a region in Figure 3a, zoomed and rotated to the appropriate direction. Since the scale bar in this figure is 1μm, the surface roughness

of sidewall was in the sub-micron regime, which makes the roughness less than one tenth of the wavelength of the propagating whispering gallery mode; hoewever, this roughness is likely the limiting factor for the Q of the current devices. The oxygen ICP RIE angle etch also produced a non-uniform undercut depth in the diamond, which could also contribute to cavity losses.

The dimensions of the diamond microdisks are shown in Figure 4. The diameters are approximately 1mm, the heights are approximately 11μm, the thicknesses of the protruding disk edges (waveguiding regions) are approximately 1μm, and the depths of the undercut of the protruding edges are around 5μm.

Optical Measurement and Fourier Analysis

The schematic diagram of the optical measurement experiment is given in Figure 5. A quantum cascade laser (QCL) (Mircat, Daylight Solutions, Inc) emitted a collimated long-wave infrared beam, which was scanned across wavelengths from 9.0μm to 9.7μm with a $0.1cm^{-1}/s$ scan rate. The laser linewidth is less than $0.1cm^{-1}$. The laser beam propagated through a chopper and focused by a BD-2 chalcogenide lens (focal length is 4mm from Thorlab, Inc.). By adjusting the location of diamond microdisk via a three-axis precision stage, the focal point was positioned at the rim of the microdisk and therefore light at the proper resonant frequencies could be coupled into the microdisk. The uncoupled light was then collected by a single-mode As_2Se_3 chalcogenide fiber (IRF-Se-12, IRflex). Finally, a Mercury Cadmium Telluride (MCT) photodetector (Electro-Optical Systems, Inc.) with a lock-in amplifier was used to record the signal at the output end of the fiber.

In this experiment, two single-crystal CVD diamond microdisks were made. Before delving into the details of the data, we should note that Figures 6 and 8 represent "control" measurements where no microdisk was present, and we were simply sending light through free space to the chalcogenide fiber. The philosophy behind the control measurements was to ensure that we were not generating spurious resonances within the basic optical apparatus of Figure 5, for example via an unintentional cavity formed from parasitic reflections. The spectrum we measured for first control measurement and the first microdisk are given in Figures 6a and 7a, respectively. In the first microresonator, whose data is shown in Figure 7, some silver-coated silica microparticles (diameter ~ 2.5μm) were spread on the surface of the microresonator as suggested in reference [78] in order to enhance the Rayleigh scattering and further boost the free-space coupling efficiency. (Note that the second microresonator whose data is shown in later in Figure 9 was not treated in this manner.) Since the wavelength range over which the LWIR laser was tuned covered

many free spectral ranges of the microresonators, we were able to use a novel Fourier analysis of the spectrum versus laser frequency scan rate. These transforms are shown in Figures 6b and 7b, for the control and microresonator measurements respectively. No peaks that could be confused with a resonance pattern were seen in the control, but with the microresonator, there is an obvious low frequency structure with a prominent peak in Figure 7b around 0.065Hz. As mentioned, this peak is missing in the control group Figure 6b. In our measurement, the scan rate was fixed at 0.1cm^{-1}/s. 0.065Hz corresponds to 15.38 seconds or 1.538cm^{-1}. The resonance condition of a whispering-gallery-mode microresonator satisfies the relationship, $m\lambda_m = n_{eff} 2\pi R$ where m is the mode number, λ_m is mode wavelength, n_{eff} is the effective refractive index, and R is the radius of microresonator. For wavelengths around 9.5μm as in our scan and using the refractive index of diamond in this range, n = 2.4, the free spectral range of diamond microdisk with perfect overlap of the whispering gallery mode with the diamond waveguide, the free spectral range is approximately 40GHz or 1.33 cm^{-1}. However, we note that perfect overlap of the mode with the diamond is highly non-physical. There will always be evanescent fields that extend into the air around the microresonator guiding ring, just as with any core cladding waveguide. This gives an effective index for the mode below that of 2.4. The measured value of the free spectral range matches this expected effective mode index. One of the resonant modes in Figure 7a is circled by black dashed line and a zoom-in of this mode is shown in the inset and the shape of the mode was fit to a quality factor simulation. For this mode, the quality factor Q is around 3648 at 9.601μm. We note that many modes had comparable values and that this mode was not unique in its properties.

The optical measurement of a second control and a second microresonator are shown in Figures 8 and 9, respectively. The dimensions of the second microdisk are very similar to the first, varying only by small microfabrication variations. As mentioned previously, there were no microparticles dispersed on the surface of this resonator. Similar measurements and analyses were performed. A Fourier transform of the control experimental spectrum is plotted in Figure 8b, showing no obvious peaks except for low frequency noise far outside the microresonator range. The Fourier transform of the microdisk spectrum in Figure 9b shows a prominent peak at 0.065Hz (Figure 9c) which closely matches the modal effective index free spectral range as in our calculation for disk 1. As before, one resonant mode is shown with a circular dashed line in Figure 9. This mode is then zoomed in a inset and curve fit for Q. The quality factor for this mode is

around 3130 at 9.541μm, comparable to the first one. We note again that many other modes of the resonator have similar properties.

Comparing the spectra of the first and second microdisks, we can conclude that the microparticles on the surface of the first microdisk did not have a major impact on coupling light into or out of this particular microresonator design. If the laser beam interacted with the microparticles, we might have observed the mode splitting because of mismatch of light travel in the clockwise and counterclockwise directions in the microdisk [69]. It may be that our microparticles were not properly position on the vertical sidewall of the microresonator to see the improved coupled that was observed in previous work.

The quality factors of these diamond microresonators far exceed the existing state of the art for an LWIR cavities. We have demonstrated the first whispering-gallery mode single-crystal diamond microdisks for the long-wave infrared. In the experiment, millimeter-size diamond disks were made by oxygen plasma ICP RIE with angled etching to create a protruding ring waveguide. The diamond microdisks have quality factors higher than 3000, exceeding prior LWIR cavity Q by more than an order of magnitude. Fourier analysis further confirmed that the measured results match the theoretically calculated free spectral range.

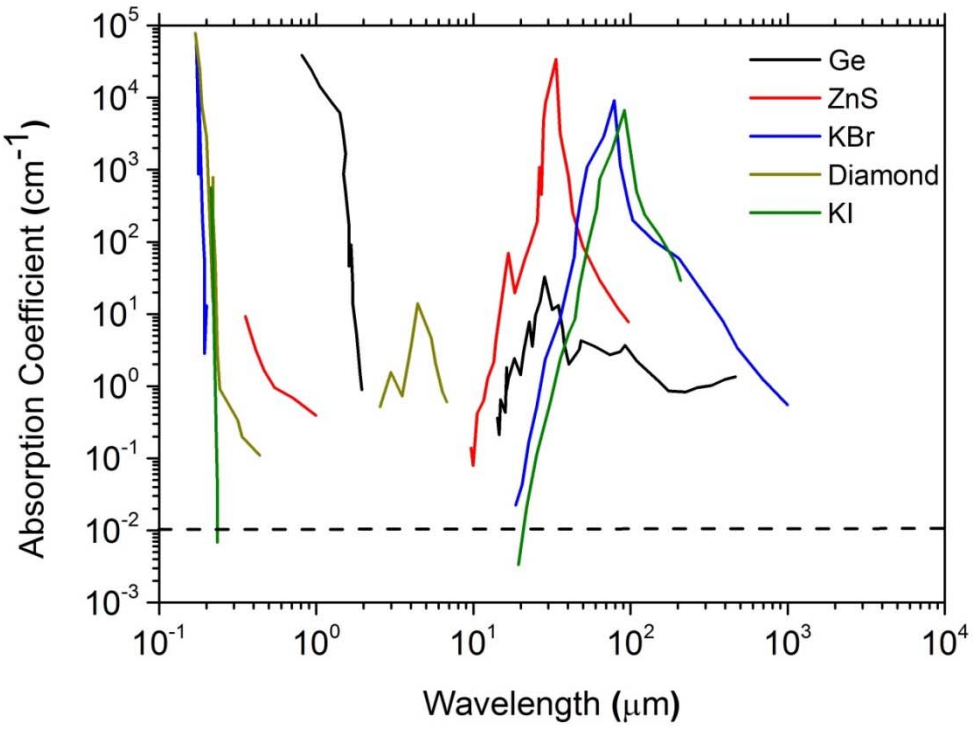

Figure 1. Absorption coefficients versus wavelength for many common infrared materials [29]. The black dashed line indicates an absorption coefficient, $\alpha = 0.01 cm^{-1}$. Using $F = \frac{\pi\sqrt{1-A}}{A}$, this corresponds to a cavity finesse of about $F = 628,000$, which is achievable in other wavelength ranges but has never been approached in the room temperature thermal infrared.

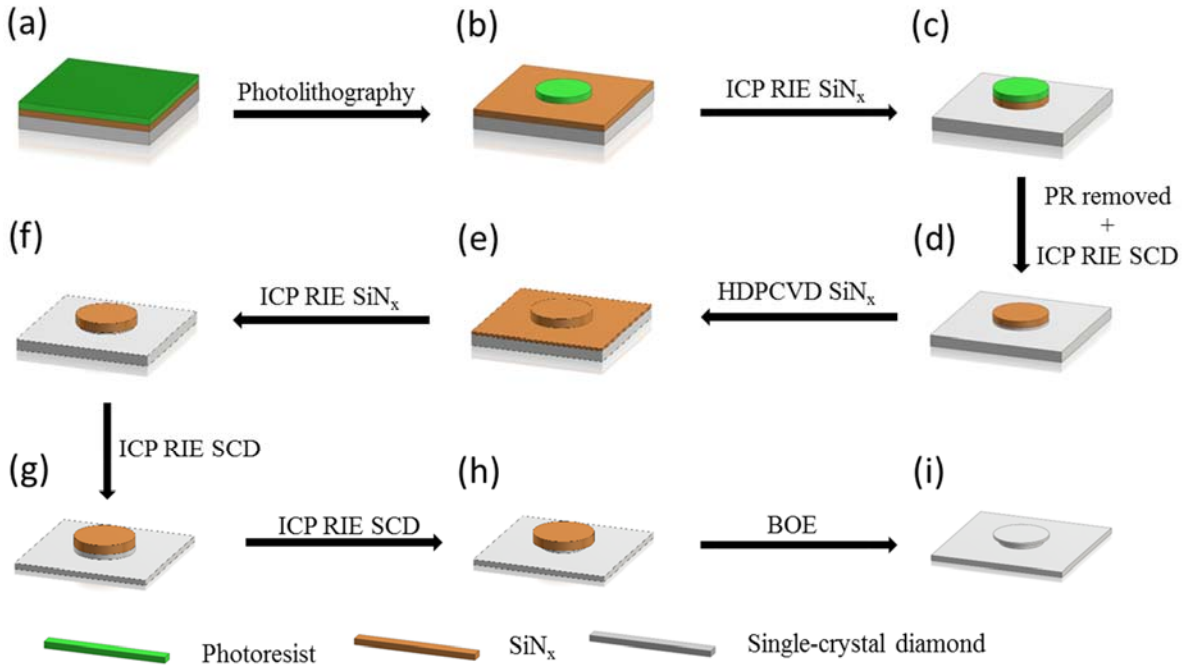

Figure 2. Fabrication process flow. (a) Silicon nitride was deposited on a diamond substrate. Photoresist was subsequently applied. (b) The photoresist was patterned using standard lithography. (c) The silicon nitride was etched by ICP RIE. (d) The diamond substrate was etched by ICP RIE. (e) Silicon nitride was deposited again. (f) The silicon nitride on the top surface was etched by ICP RIE, which left residual silicon nitride on the sidewall. (g) The diamond was etched again by ICP RIE to create the desired microresonator height. (h) The diamond substrate was mounted vertically and etched at a high angle by ICP RIE to create an undercut. (i) The rest of the silicon nitride was removed by a buffered oxide etch. Acronyms used in the diagram: PR: photoresist, SiN_x: silicon nitride, SCD: single-crystal diamond, ICP RIE: inductively coupled plasma reactive ion etching, HDPCVD: high density plasma chemical vapor deposition, and BOE: buffered oxide etch.

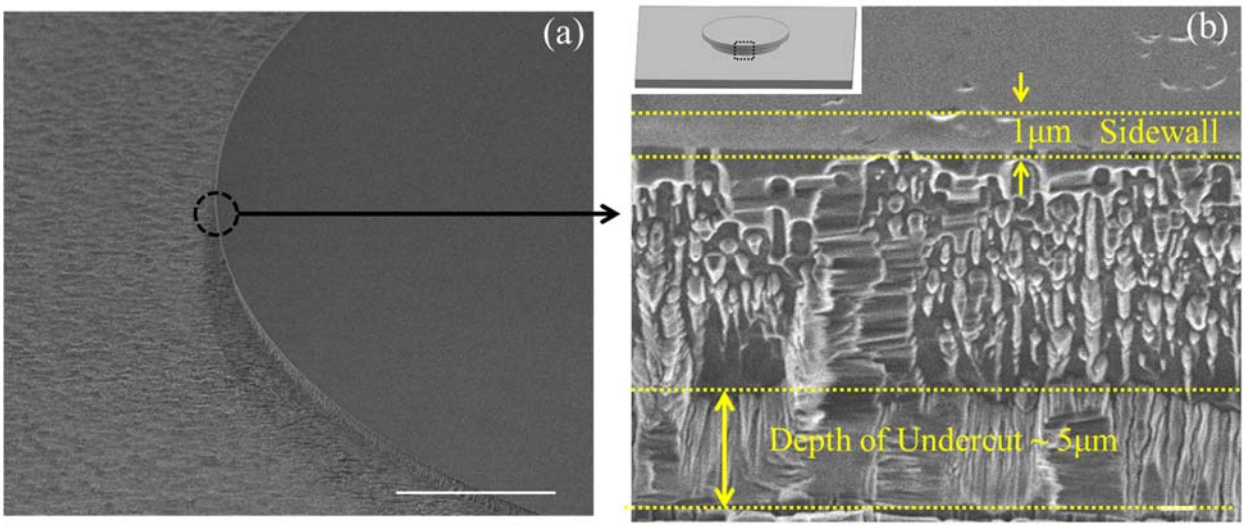

Figure 3 SEM images of diamond microdisk. SEM images of the cross-sectional views of diamond microdisk were taken with a tilt angle of 75 degrees. Scale bars in (a) and (b) are 100μm and 1μm, respectively. Note that the 1μm sidewall is the disk ring waveguide, and it is a smooth surface that protrudes from the rough sidewall by about 5μm.

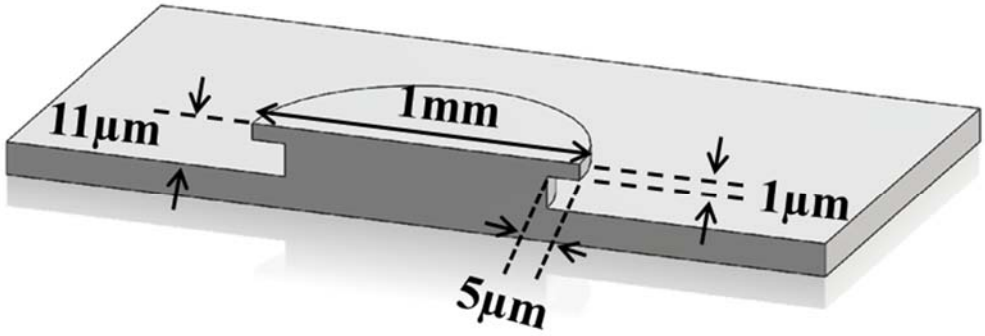

Figure 4 - Dimensions of microresonator (cross-sectional view). The diameters of the diamond microresonators were 1mm with a height of 11μm. The thickness of the protruding disk waveguide was 1μm, and the depth of undercut was approximately 5μm.

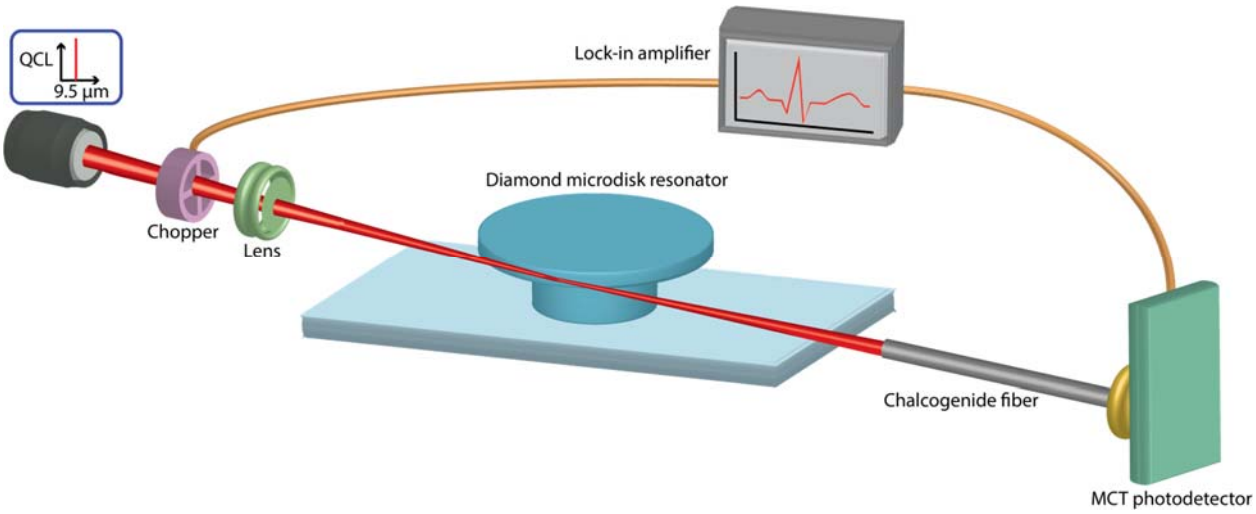

Figure 5 - Optical measurement setup. An experimental setup consisting of a tunable quantum cascade laser (QCL) (λ~9–10 μm) coupled to a single-crystal diamond microdisk was used. The uncoupled light was collected by a single-mode As_2Se_3 chalcogenide fiber, and was detected by a Mercury Cadmium Telluride (MCT) photodetector with a lock-in amplifier to record the signal.

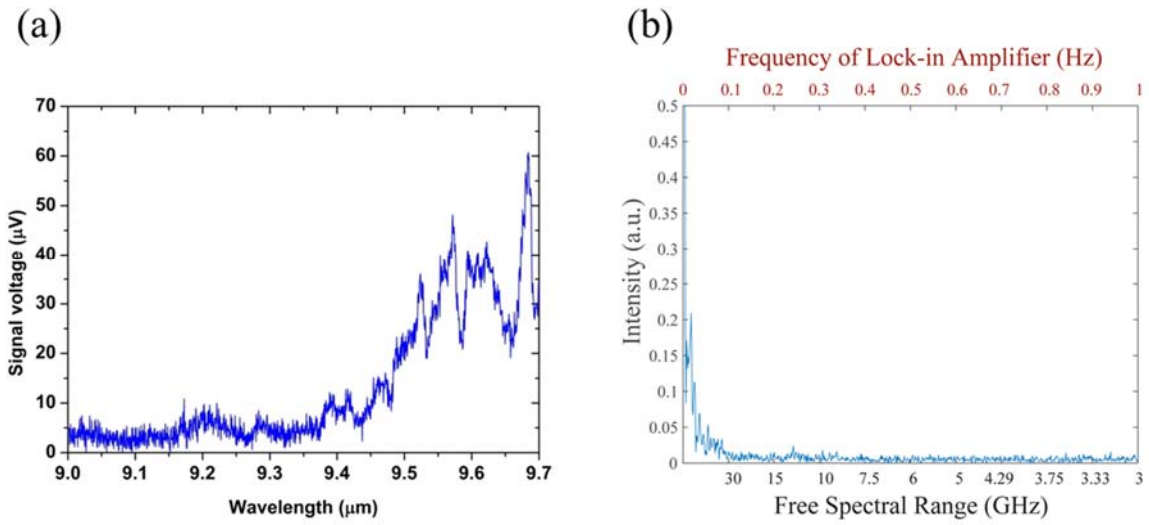

Figure 6 Control measurement prior to insertion of microresonator 1. a. Optical measurement using the experimental set-up of Figure 5 but without a microresonator. The purpose of this experiment was to ensure that there were no spurious parasitic cavities in the optical set-up that would interfere in the microresonator analysis. Part (b) is a Fourier transform of the data in (a). In (b), the x-axis on the bottom is the free spectral range when scan rate of tunable laser is at $0.1 cm^{-1}/s$. The x-axis on the top (red) is the sampling rate of

the lock-in amplifier.

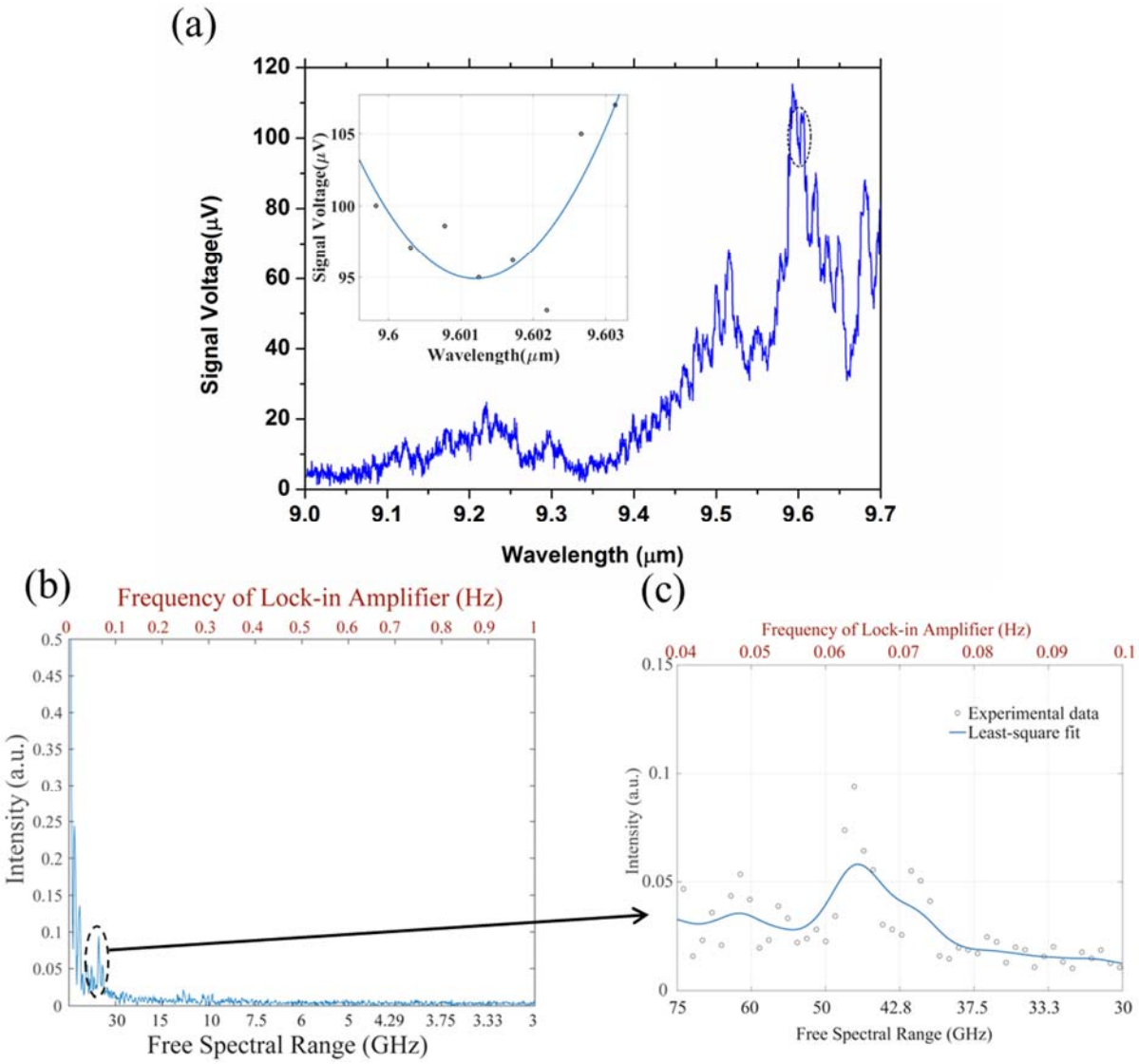

Figure 7 – Spectral analysis of microresonator 1. Part (a) is the intensity versus wavelength plot for the first diamond microresonator. Inset: Expanded view of the experimental data circled by the black dashed line in (a) The blue line is a curve fit. The quality factor for this sample is 3648 at 9.601μm. Part (b) is a Fourier transform of the data in (a). There is an obvious peak around 40GHz and and an expansion in is shown in (c) with curve fitting. In (b) and (c), the x-axes on the bottom are the free spectral ranges when the scan rate of tunable laser is at 0.1cm^{-1}/s. The x-axes on the top (red) are the sampling rate of the lock-in amplifier.

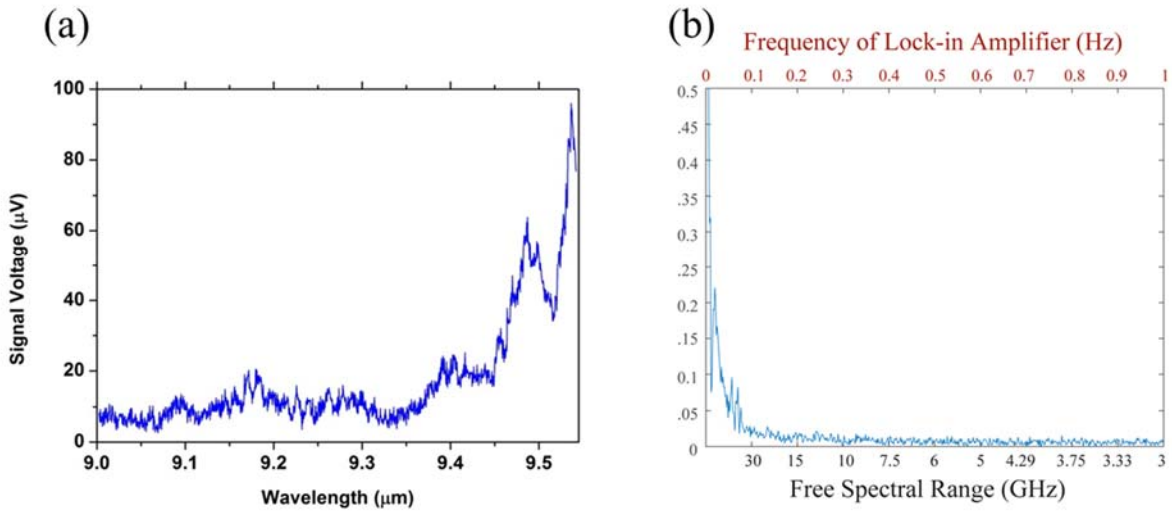

Figure 8 Optical measurement for the control group of the second diamond microdisk.
a. Optical measurement setting as Figure 5 but the second diamond microdisk was missing. b. Fourier transform of (a). In (b), the x-axis on the bottom is the free spectral range when scan rate of tunable laser is at 0.1cm^{-1}/s. The x-axis on the top (red) is the sampling rate of the lock-in amplifier.

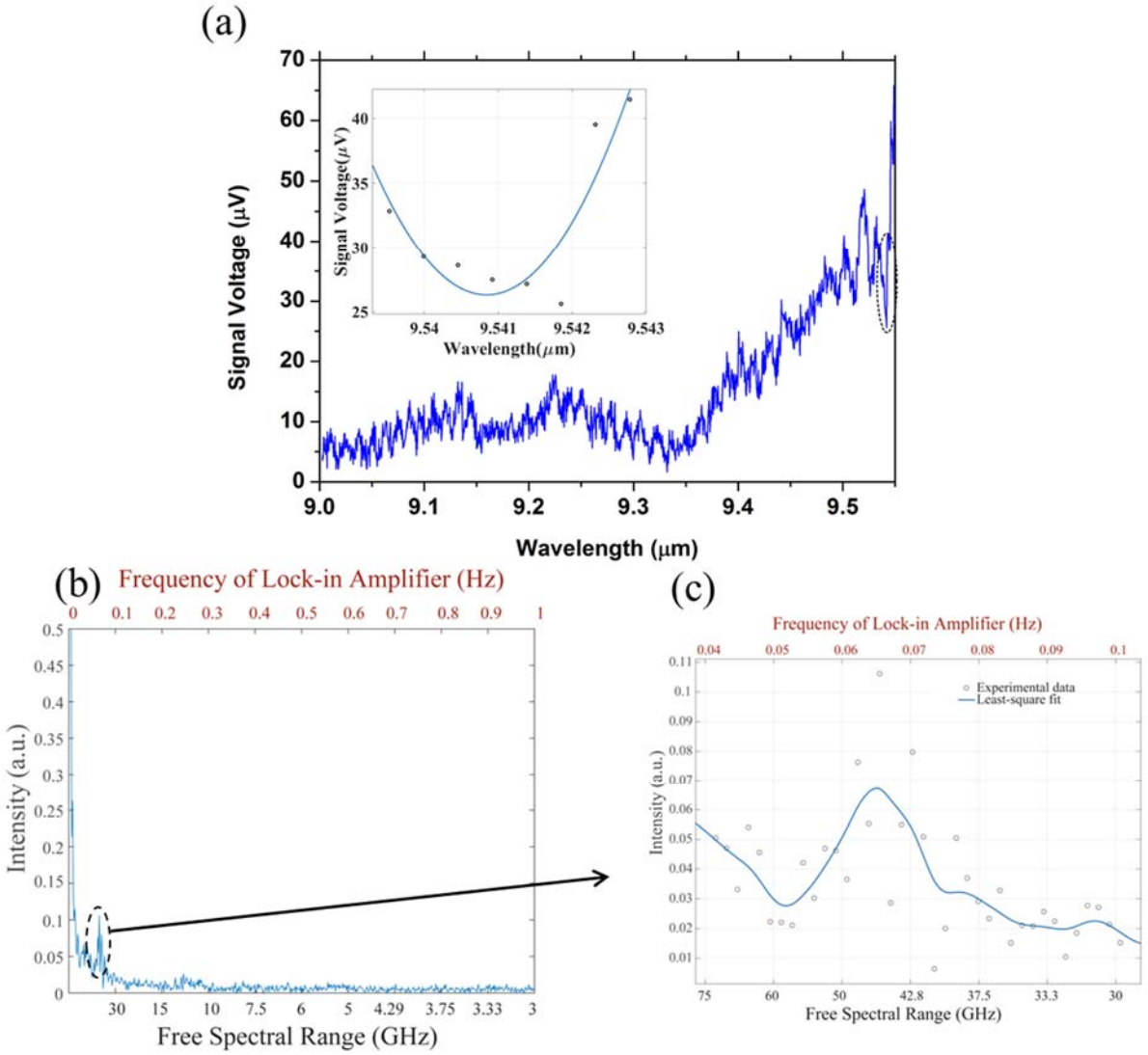

Figure 9 Optical measurement for the experimental group of the second microdisk. a. Optical measurement of the first diamond microdisk. Inset: the zoom in of experiment data circled by black dash line. Curve fitting is given by blue line. Quality factor for this sample is around 3130 at 9.541μm. b. Fourier transform of (a). There is an obvious peak around 40GHz and its zoom in is shown in (c) with curve fitting. In (b) and (c), the x-axes on the bottom are the free spectral ranges when scan rate of tunable laser is at 0.1cm^{-1}/s. The x-axes on the top (red) are the sampling rate of the lock-in amplifier.

REFERENCES

[1] K. Olson and J. Talghader "Spectrally dependent fluctuations of thermal photon sources, *Physical Review A*, vol. 94, 013822, 5 pages, 2016.

[2] Y. J. Lee and J. J. Talghader, "Observational limitations of Bose-Einstein photon statistics and radiation noise in thermal emission," *Physical Review A*, vol. 97, 013844 (11 pages), 26 January 2018. DOI: 10.1103/PhysRevA.97.013844

[3] A. S. Gawarikar, R. P. Shea, and J. J. Talghader, *IEEE Trans. Electron Devices* **60**, 2586 (2013).

[4] J. J. Talghader, A. S. Gawarikar, and R. P. Shea, *Light Sci. Appl.* **1**, e24 (2012).

[5] J.-J. Greffet, R. Carminati, K. Joulain, J.-P. Mulet, S. Mainguy, and Y. Chen, *Nature* **416**, 61 (2002).

[6] Y. Wang, B. J. Potter, and J. J. Talghader, *Opt. Lett.* **31**, 1945 (2006).

[7] X. Liu, T. Tyler, T. Starr, A. F. Starr, N. M. Jokerst, and W. J. Padilla, *Phys. Rev. Lett.* **107**, 045901 (2011).

[8] B. J. Lee and Z. M. Zhang, *J. Heat Transfer* **129**, 17 (2007).

[9] B. J. Lee, L. P. Wang, and Z. M. Zhang, *Opt. Express* **16**, 11328 (2008).

[10] M. Laroche, R. Carminati, and J.-J. Greffet, *Phys. Rev. Lett.* **96**, 123903 (2006).

[11] A. L. Marshall and F. J. Norton, *J. Am. Chem. Soc.* **72**, 2166 (1950).

[12] I. Celanovic, D. Perreault, and J. Kassakian, *Phys. Rev. B* **72**, 075127 (2005).

[13] R. W. Boyd, *Infrared Phys.* **22**, 157 (1982).

[14] R. J. Thompson, G. Rempe, and H. J. Kimble, *Phys. Rev. Lett.* **68**, 1132 (1992).

[15] P. Maunz, T. Puppe, I. Schuster, N. Syassen, P. W. H. Pinkse, and G. Rempe, *Nature* **428**, 50 (2004).

[16] C. J. Hood, *Science* **287**, 1447 (2000).

[17] P. Goy, J. M. Raimond, M. Gross, and S. Haroche, Phys. Rev. Lett. **50**, 1903 (1983).

[18] P. R. Rice and H. J. Carmichael, IEEE J. Quantum Electron. **24**, 1351 (1988).

[19] R. Miller, T. E. Northup, K. M. Birnbaum, A. Boca, A. D. Boozer, and H. J. Kimble, J. Phys. B At. Mol. Opt. Phys. **38**, S551 (2005).

[20] H. Walther, B. T. H. Varcoe, B.-G. Englert, and T. Becker, Reports Prog. Phys. **69**, 1325 (2006).

[21] L. Mandel, Proc. Phys. Soc. **74**, 233 (1959).

[22] H. P. Baltes, Infrared Phys. **16**, 1 (1976).

[23] P. B. Fellgett, J. Opt. Soc. Am. **39**, 970 (1949).
[24] R. C. Jones, J. Opt. Soc. Am. **37**, 879 (1947).
[25] W. B. Lewis, Proc. Phys. Soc. **59**, 34 (1947).
[26] M. Fox, *Quantum Optics: An Introduction* (Oxford University Press, 2006).
[27] L. Mandel and E. Wolf, *Optical Coherence and Quantum Optics* (Cambridge University Press, 1995).
[28] C. M. Caves, Phys. Rev. Lett. **45**, 75 (1980).
[29] W. A. Edelstein, J. Hough, J. R. Pugh, and W. Martin, J. Phys. E. **11**, 710 (1978).

[30] S. J. C. Yates, J. J. A. Baselmans, A. Endo, R. M. J. Janssen, L. Ferrari, P. Diener, and A. M. Baryshev, Appl. Phys. Lett. **99**, 073505 (2011).
[31] P. J. de Visser, J. J. A. Baselmans, J. Bueno, N. Llombart, and T. M. Klapwijk, Nat. Commun. **5**, 3130 (2014).
[32] J. Hubmayr, J. Beall, D. Becker, H.-M. Cho, M. Devlin, B. Dober, C. Groppi, G. C. Hilton, K. D. Irwin, D. Li, P. Mauskopf, D. P. Pappas, J. Van Lanen, M. R. Vissers, Y. Wang, L. F. Wei, and J. Gao1, Appl. Phys. Lett. **106**, 073505 (2015).
[33] S. R. Andrews and B. A. Miller, J. Appl. Phys. **70**, 993 (1991).
[34] A. Reiser and L. Schachter, Phys. Rev. A **87**, 033801 (2013).
[35] S. M. Rytov, Theory of Electric Fluctuations and Thermal Radiation (Air Force Cambridge Research Center, Bedford, 1959).
[36] R. W. Boyd, Infrared Phys. **22**, 157−162 (1982).
[37] S. Gulkis, TDA Prog. Rep. **42-71**, 53−59 (1982).
[38] R. C. Jones, J. Opt. Soc. Am. **37**, 879–888 (1947).
[39] P. B. Fellgett, J. Opt. Soc. Am. **39**, 970–976 (1949).
[40] W. B. Lewis, Proc. Phys. Soc. **59**, 34–40 (1947).
[41] P. Fellgett, C. Jones, and R. Q. Twiss, Nature **4691**, 967−969 (1959).
[42] M. Planck, Annalen der Physik **306**, 719–737 (1901).
[43] P. L. Richards, J. Appl. Phys. **76**, 1 (1994).
[44] P. W. Kruse, L. D. McGlauchlin, and R. B. McQuistan, Elements of Infrared Technology (Wiley, 1962).
[45] E. L. Dereniak and G. D. Boreman, Infrared Detectors and Systems (Wiley-Interscience, 1996).
[46] J. J. Talghader, A. S. Gawarikar, and R. P. Shea, Light Sci. Appl. **1**, e24 (2012).
[47] C. Wuttke and A. Rauschenbeutel, Phys. Rev. Lett. **111**, 024301 (2013).

[48] D. J. Benford, T. R. Hunter, and T. G. Phillips, Int. J. Infrared Millimeter Waves **19**, 931–938 (1998).
[49] K. Olson and J. Talghader, Phys. Rev. A **94**, 013822 (2016).
[50] P. Del'Haye, A. Schliesser, O. Arcizet, T. Wilken, R. Holzwarth and T. J. Kippenberg, Nature **450**, 1214 – 1214 (2007).
[51] T.-J. Wang, J.-Y. He, C.-A. Lee, and H. Niu, Opt. Express **27**, 28119−28124 (2012).
[52] M. Furchi, A. Urich, A. Pospischil, G. Lilley, K. Unterrainer, H. Detz, P. Klang, A. M. Andrews, W. Schrenk, G. Strasser, and T. Mueller, Nano Lett. **12**, 2773−2777 (2012).
[53] Y. Wang, B. J. Potter, and J. J. Talghader, Opt. Lett. **31**, 1945−1947 (2006).
[54] D. Kirikae, Y. Suzuki1 and N. Kasagi, J. Micromech. Microeng. **20**, 104006 (2010).
[55] Z. Su, N. Li, E. S. Magden, M. Byrd, Purnawirman, T. N. Adam, G. Leake, D. Coolbaugh, J. D. B. Bradley, and M. R. Watts, Opt. Lett. **41**, 5708−5711 (2016).
[56] Z. Qian, S. Kang, V. Rajaram, and M. Rinaldi, 2016 IEEE Sensors, 625−627.
[57] T. D. Dao, S. Ishii, T. Yokoyama, T. Sawada, R. P. Sugavaneshwar, K. Chen, Y. Wada, T. Nabatame, and T. Nagao, ACS Photonics **3**, 1271−1278 (2016).
[58] L. Mandel and E. Wolf, Optical Coherence and Quantum Optics (Cambridge University Press, 1995).
[59] M. Fox, Quantum Optics: An Introduction (Oxford University Press, 2006).
[60] C. Lecaplain1, C. Javerzac-Galy, M.L. Gorodetsky, and T.J. Kippenberg, Nat. Commun. **7**, 13383 (2016).
[61] A. Rasoloniaina, V. Huet, T. K. N. Nguyên, E. Le Cren, M. Mortier, L. Michely, Y. Dumeige & P. Féron, Sci. Rep. **4**, 4023 (2014).
[62] P. Ma, D.-Y. Choi, Y. Yu, Z. Yang, K. Vu, T. Nguyen, A. Mitche, B. Luther-Davies, and S. Madden, Opt. Express **23**, 19969−19979 (2015).
[63] K. Olson, High Power Continuous Wave Laser Heating and Damage with Contamination, and Non-Uniform Spectrally Dependent Thermal Photon Statistics (Doctoral Dissertation, University of Minnesota, 2015).

[64] Liu, X. et al. Ultra-high-Q UV microring resonators based on a single-crystalline AlN platform. *Optica* **5**, 1279–1282 (2018).
[65] Liu, X. et al. Aluminum nitride-on-sapphire platform for integrated high-Q microresonators. *Opt. Express* **25**, 587–594 (2017).
[66] Giorgini, A., Avino, S., Malara, P., De Natale, P. & Gagliardi, G. Fundamental limits in high-Q droplet microresonators. *Sci. Rep.* **7**, 41997 (2017).

[67] Wang, L. et al. Frequency comb generation in the green using silicon nitride microresonators. Laser Photonics Rev. **10**, 631–638 (2016).

[68] Javerzac-Galy, C. et al. Excitonic Emission of Monolayer Semiconductors Near-Field Coupled to High-Q Microresonators. *Nano Lett.* **18**, 3138–3146 (2018).

[69] Zhu, J. et al. On-chip single nanoparticle detection and sizing by mode splitting in an ultrahigh-Q microresonator. *Nat. Photonics* **4**, 46–49 (2010).

[70] Jiang, X. et al. Chaos-assisted broadband momentum transformation in optical microresonators. *Science* **358**, 344–347 (2017).

[71] Kippenberg, T. J., Spillane, S. M. & Vahala, K. J. Kerr-nonlinearity opticalparametric oscillation in an ultrahigh-Q toroid microcavity. *Phys. Rev. Lett.* **93**, 083904 (2004).

[72] Armani, D. K., Kippenberg, T. J., Spillane, S. M., Vahala, K. J. Ultra-high-Q toroid microcavity on a chip. *Nature* **421**, 925–928 (2003).

[73] Del'Haye, P. et al. Optical frequency comb generation from a monolithic microresonator. *Nature* **450**, 1214–1217 (2007).

[74] Khanaliloo, B., Mitchell, M., Hryciw, A. C., Barclay, P. E. High-Q/V monolithic diamond microdisks fabricated with quasi-isotropic etching. *Nano Lett.* **15**, 5131–5136 (2015).

[75] Song, B.-S. et al. Ultrahigh-Q photonic crystal nanocavities based on 4H silicon carbide. *Optica* **6**, 991–995 (2019).

[76] Yang, K. Y. et al. Bridging ultrahigh-Q devices and photonic circuits. *Nat. Photonics* **12**, 297–302 (2018).

[77] Lin, J. et al. Fabrication of high-Q lithium niobate microresonators using femtosecond laser micromachining. *Sci. Rep.* **5**, 8072 (2015).

[78] Zhu, J. et al. Interfacing whispering-gallery microresonators and free space light with cavity enhanced Rayleigh scattering. *Sci. Rep.* **4**, 6396 (2014).

[79] Rasoloniaina, A. et al. Controling the coupling properties of active ultrahigh-Q WGM microcavities from undercoupling to selective amplification. *Sci. Rep.* **4**, 4023 (2014).

[80] Schneider, C., Gold, P., Reitzenstein, S., Höfling, S., Kamp, M. Quantum dot micropillar cavities with quality factors exceeding 250,000. *Appl. Phys. B* **122**, 1–6 (2016).

[81] Xuan, Y. et al. High-Q silicon nitride microresonators exhibiting low-power frequency comb initiation. *Optica* **3**, 1171–1180 (2016).

[82] Marin-Palomo, P. et al. Microresonator-based solitons for massively parallel coherent optical communications. *Nature* **546**, 274–279 (2017).

[83] Wachter, G. et al. Silicon microcavity arrays with open access and a finesse of half a

million. *Light Sci. Appl.* **8**, 37 (2019).

[84] Lecaplain, C., Javerzac-Galy, C., Gorodetsky, M. L. & Kippenberg, T. J. Mid-infrared ultra-high-Q resonators based on fluoride crystalline materials. *Nat. Commun.* **7**, 13383 (2016).

[85] Grudinin, I. S., Mansour, K. & Yu, N. Properties of fluoride microresonators for mid-IR applications. *Opt. Lett.* **41**, 2378–2381 (2016).

[86] Way, B., Jain, R. K. & Hossein-Zadeh, M. High-Q microresonators for mid-IR light sources and molecular sensors. *Opt. Lett.* **37**, 4389–4391 (2012).

[87] Mao, H. et al. Ge/ZnS-based micromachined Fabry–Perot filters for optical MEMS in the longwave infrared. *IEEE Journal of Microelectromechanical Systems* **24**, 2109–2115 (2015).

[88] Tuohiniemi, M., Näsilä, A. & Mäkynen, J. Characterization of the tuning performance of a micro-machined Fabry–Pérot interferometer for thermal infrared. *J. Micromech. Microeng.* **23**, 075011 (2013).

[89] Mao, H. et al. Large-area MEMS tunable Fabry–Perot filters for multi/hyperspectral infrared imaging. *IEEE J. Sel. Top. Quant.* **23**, 2700208 (2017).

[90] Neumann, N. at el. Uncooled IR sensors with tunable MEMS Fabry-Pérot filters for the long-wave infrared range. 2010 IEEE Sensors, 2383–2387.

[91] Meinig, M. et al. Dual-band MEMS Fabry-Pérot filter with two movable reflectors for mid- and long-wave infrared microspectrometers. Solid-State Sensors Actuators and Microsystems Conference (TRANSDUCERS) 2011 16th International, 2538–2541.

[92] Palik, E. D. *Handbook of Optical Constants of Solids* (Academic Press, Cambridge, MA, 1997).

[93] Burek, M. J. et al. High quality-factor optical nanocavities in bulk single-crystal diamond. *Nat. Commun.* **5**, 5718 (2014).

[94] Burek, M. J. et al. Free-Standing Mechanical and Photonic Nanostructures in Single-Crystal Diamond. *Nano Lett.* **12**, 6084−6089 (2012).

[95] Hausmann, B. J. M. et al. Fabrication of diamond nanowires for quantum information processing applications. *Diam. Relat. Mater.* **19**, 621–629 (2010).

[96] Mitchell, M. et al. Single-crystal diamond low-dissipation cavity optomechanics. *Optica* **3**, 963–970 (2016).

[97] Hwang, K. D. S., Saito, T. & Fujimori, N. New etching process for device fabrication using diamond. *Diam. Relat. Mater.* **13,** 2207–2210 (2004).

[98] Tao, Y., Boss, J. M., Moores, B. A. & Degen, C. L. Single-crystal diamond

nanomechanical resonators with quality factors exceeding one million. *Nat. Commun.* **5**, 3638 (2014).

[99] Faraon, A., Barclay, P. E., Santori, C., Fu, K.-M. C. & Beausoleil, R. G. Resonant enhancement of the zero-phonon emission from a colour centre in a diamond cavity. *Nat. Photonics* **5**, 301–305 (2011).

[100] Graziosi, T., Mi, S., Kiss, M. & Quack, N. Single crystal diamond micro-disk resonators by focused ion beam milling. *APL Photonics* **3**, 126101 (2018).

[101] Ilchenko, V. S. et al. Whispering gallery mode diamond resonator. *Opt. Lett.* **38**, 4320–4323 (2013).

[102] Hausmann, B. J. M. et al. Integrated High-Quality Factor Optical Resonators in Diamond. *Nano Lett.* **13**, 1898–1902 (2013).

[103] Bayer, M. M., Çirkino˘glu, H. O. & Serpengüzel, A. Observation of whispering-gallery modes in a diamond microsphere. *IEEE Photonics Technology Letters,* **30**, 3–6 (2018).